N 62 10021

NASA TN D-981

NASA TN D-981

TECHNICAL NOTE

D-981

AERODYNAMIC CHARACTERISTICS OF A POWERED SEMISPAN TILTING-SHROUDED-PROPELLER VTOL MODEL IN HOVERING AND TRANSITION FLIGHT

By Kenneth W. Goodson and Kalman J. Grunwald

Langley Research Center
Langley Air Force Base, Va.

NATIONAL AERONAUTICS AND SPACE ADMINISTRATION

WASHINGTON January 1962

1Y

NATIONAL AERONAUTICS AND SPACE ADMINISTRATION

TECHNICAL NOTE D-981

AERODYNAMIC CHARACTERISTICS OF A POWERED SEMISPAN TILTING-SHROUDED-PROPELLER VTOL MODEL IN HOVERING AND TRANSITION FLIGHT

By Kenneth W. Goodson and Kalman J. Grunwald

L
1
5
6
5

SUMMARY

An investigation of the aerodynamic characteristics of a powered semispan tilting-shrouded-propeller configuration has been conducted in the 17-foot test section of the Langley 300-MPH 7- by 10-foot tunnel. The wing had an aspect ratio of 2.67 (based on wing span of 60 inches), a taper ratio of 0.67, and an NACA 2418 airfoil section with a 15-inch-diameter shrouded propeller mounted on the tip.

The test results show that large nose-up pitching moments are obtained at transitional speeds of about 40 knots and duct angle of about 70°. Decelerating flight produces further increases in the nose-up moment. Ground proximity reduces the nose-up pitching moments. The large nose-up moments can be trimmed by use of duct-exit control vanes.

The results show that unloading the duct (shroud) by flying at a wing angle of attack of 15° reduces the power required by about 30 percent at 50 knots. Duct-lip stall produces large increases in power required. The results in general show that full-scale aerodynamic simulation can be made with small-scale wind-tunnel models if duct-lip separation at low Reynolds numbers is avoided.

INTRODUCTION

The ducted (shrouded) propeller has frequently been proposed as a device for lifting VTOL airplanes because of the possible reduction in propeller diameter for a given static thrust as compared with an unshrouded propeller. Considerable research has been done on the static characteristics of ducted (shrouded) propellers, but relatively little data are available on the characteristics of ducted-fan-supported VTOL aircraft at transition speeds from hovering to wing-supported flight. The present investigation on a semispan model was undertaken to determine the longitudinal stability, control, and

performance characteristics of a wing-tip-mounted ducted-propeller configuration in the hovering and transition speed range.

The investigation was conducted in the 17-foot test section of the Langley 300-MPH 7- by 10-foot tunnel and covered a range of duct angles and power conditions from hovering to forward flight. Some tests were made in the region of ground effect. An analysis of the more significant aerodynamic characteristics is presented. Duct-alone aerodynamic characteristics of the present duct are presented in reference 1.

L
1
5
6
5

SYMBOLS

The positive sense of forces, moments, and angles is shown in figure 1. The center of gravity about which the moments were taken is shown in figure 2.

A	axial force, lb
A_g	geometric aspect ratio
b_t	overall span (includes ducts), ft
y	spanwise distance from wing root chord, ft
$\bar{c}$	wing mean aerodynamic chord, ft
S	wing area (model, full span 9.37 sq ft, based on wing only)
C_L	lift coefficient, L_m/qS
A_E	duct exit area, sq ft
A_e	effective aspect ratio
η_s	static thrust efficiency
C_m	pitching-moment coefficient, $M_{Y,m}/qS\bar{c}$
C_X	longitudinal-force coefficient, X_m/qS
D	model propeller diameter, 1.25 ft
g	gravitational units, 32.2 ft/sec^2

h	ground height from duct pivot, ft
$h/\bar{c}$	nondimensional ground height based on wing chord
l_a	characteristic length of airplane, ft
l_m	characteristic length of model, ft
W_a	weight of airplane, lb
L	lift (airplane), lb
L_m	lift (model, full span), lb
$M_{x,r}$	root bending moment of airplane (see fig. 1), ft-lb
M_Y	pitching moment (airplane), ft-lb
$M_{Y,m}$	pitching moment (model, full span), ft-lb
$M_{z,r}$	root bending moment of airplane (see fig. 1), ft-lb
N	normal force, lb
n	revolutions per second of model propeller
P	power (airplane), hp
P_m	power (model, full span; 2 propellers), hp
q_o	free-stream dynamic pressure, lb/sq ft
q	dynamic pressure at vanes (possible tail locations), lb/sq ft
q/q_o	ratio of dynamic pressure at downwash vanes to free-stream dynamic pressure
T	thrust, lb
V	free-stream velocity (airplane), ft/sec
V_k	velocity (airplane), knots
V_m	free-stream velocity (model), ft/sec

X	longitudinal force (airplane), lb
X_m	longitudinal force (model, full span), lb
α	angle of attack (wing), deg
δ	duct deflection relative to wing chord line, deg
ϵ	downwash angle, deg
β	propeller blade angle at 0.75 radius station
C_P	power coefficient, $2\pi Qn/\rho n^3 D^5$
Q	model propeller shaft torque (per propeller), ft-lb
ρ	density, slugs/cu ft

L
1
5
6
5

MODEL

A drawing of the model with pertinent dimensions is shown in figure 2, and a photograph of the model mounted in the test section is shown as figure 3. A sketch showing downwash vane location is presented in figure 4. The wing employed an NACA 2418 airfoil and had an aspect ratio of 2.67 (based on wing span of 60 inches) and a taper ratio of 0.67. The wing and duct were constructed of wood and steel. The duct was attached at the tip of the steel wing spar. The duct ordinates are presented in table I. The duct could be rotated through 360° about the 0.25 wing chord line and locked in place with set screws at any angle required. Duct-lip modifications and duct exit vanes are shown in figure 5. The model duct had the same airfoil section as the duct of references 2 and 3 but had a smaller number of exit stators, no inlet vanes, and only a three-blade propeller. The model was pivoted about the duct 44-percent-chord position whereas the airplane was pivoted about the duct 55-percent-chord position.

Free-floating vanes were placed behind the model on the tunnel floor (figs. 3 and 4) to determine the flow field in the region of a possible horizontal tail. Each downwash vane (fig. 4) had total-pressure tubes located in its leading edges which were connected to a small plenum chamber from which the average pressure across the tail span could be measured to determine the dynamic pressure at the tail. (See ref. 4 for more detail.) These pressures and local wind directions were measured by a pressure transducer and a slide-wire potentiometer and displayed on a chart recorder.

The 8-foot by 8-foot groundboard was located at heights of 17 inches and 34 inches from the duct pivot point which gives a duct exit height of 11.22 and 28.22 inches, respectively, from the duct trailing edge when the duct is deflected 90°.

The forces and moments of the model were measured on a five-component strain-gage balance mounted below the floor of the tunnel. The model power was obtained by measuring minimum current and using the motor torque calibration. The propeller blade angle was set at 24° at the 0.75 radius station. The model propeller design characteristics are presented in reference 1.

L
1
5
6
5

TESTS AND CORRECTIONS

The test procedure in the tunnel consisted of setting the propeller rotational speed (at 8,000 revolutions per minute where possible, 6,000 for other conditions) with the model at zero angle of attack and at a given duct (shroud) angle and then increasing the tunnel speed until zero longitudinal force was obtained. This tunnel speed, which corresponded to the condition of steady level flight at an angle of attack of 0°, was held constant as the data were taken through an angle-of-attack range. A similar procedure was used to simulate accelerating and decelerating flight conditions by testing at tunnel speeds above and below the speed for steady level flight. The only correction applied to the data was a flow-alinement correction to the angle of attack of 1.25°.

PRESENTATION OF RESULTS

Data obtained through a hovering to cruise speed range lose their significance when presented in the standard or conventional coefficient form based on free-stream dynamic pressure, since coefficients become infinitely large as the hovering condition (zero dynamic pressure) is approached. In order to make the present data more understandable, only the data obtained at high speeds (speeds near which wing lift can support the aircraft) are presented in coefficient form. Data obtained at the lower free-stream dynamic pressures where the shrouded propeller contributes largely to the lift and where longitudinal equilibrium conditions ($X = 0$) can be established (hovering through transition) are presented as force and moments. Because the tests were made under varying tunnel conditions, the model force and moment data have been scaled to a common level by assuming the model to be a 5/16-scale model of an airplane and by assuming a full-scale lift of 3,000 pounds at zero angle of attack.

Results of the 5/16-scale model were scaled to the assumed 3,000-pound full-scale aircraft by using the following equations which are based on the assumption that model lift coefficients and full-scale lift coefficients are equal:

$$V = V_m \frac{l_m}{l_a} \sqrt{\frac{W_a}{L_{m(\alpha=0)}}} = V_m \frac{5}{16} \sqrt{\frac{3,000}{L_{m(\alpha=0)}}}$$

$$L = L_m \frac{W_a}{L_{m(\alpha=0)}} = L_m \frac{3,000}{L_{m(\alpha=0)}}$$

L
1
5
6
5

$$X = X_m \frac{W_a}{L_{m(\alpha=0)}} = X_m \frac{3,000}{L_{m(\alpha=0)}}$$

$$M_Y = M_{Y,m} \frac{l_a}{l_m} \frac{W_a}{L_{m(\alpha=0)}} = M_{Y,m} \frac{16}{5} \frac{3,000}{L_{m(\alpha=0)}}$$

$$P = P_m \frac{l_m}{l_a} \left(\frac{W_a}{L_{m(\alpha=0)}}\right)^{3/2} = P_m \frac{5}{16} \left(\frac{3,000}{L_{m(\alpha=0)}}\right)^{3/2}$$

The full-scale data presented herein can be scaled to any other size airplane by treating the present data as model data in these equations and using the appropriate scaling factor l_m/l_a and the new airplane weight W_a for a given angle of attack.

The experimental results are presented in the following figures:

	Figure
Basic transition-speed-range flight characteristics:	
Force and moment data at large duct angles (3-inch lip modification)	6
Coefficient data at small duct angles (original duct)	7
Accelerating and decelerating flight (3-inch lip modification)	8 and 9
Effect of duct exit vane deflection; $\delta = 60^{\circ}$ (original duct)	10
Transition-speed-range data with original duct	11
Effect of duct-lip modification and exit vanes; $\delta = 60^{\circ}$	12

Figure

Analysis of basic aerodynamic and performance characteristics at zero angle of attack through the transition speed range:
Effect of flight condition (acceleration) 13
Comparison of model and full-scale values 14
Spanwise center-of-pressure and horsepower variation at constant angles of attack 15
Effect of ground proximity 16
Effect of duct-lip stall (lip modification) at transition speeds 17
Dynamic-pressure ratios and downwash angles in the region of a possible tail location . . . . . 18 to 21

L
1
5
6
5

DISCUSSION

The aerodynamic and performance characteristics for equilibrium conditions in hovering through transition speeds (large duct angles) are presented as forces and moments inasmuch as the low dynamic pressures involved would make coefficients extremely large and of little value in the usual sense. However, for low duct (shroud) angles (large dynamic pressures) where tunnel conditions did not allow the obtaining of equilibrium data, the data are presented in coefficient form. The basic transition speed range force and moment data are presented in figure 6, whereas the basic-cruise or low-duct-angle-coefficient data are presented in figure 7.

Analysis figures showing the duct angle, power required, and tail-off pitching moment experienced by an assumed airplane in steady level flight, accelerating and decelerating transition in level flight both in and out of ground effect are presented in figures 13 to 16.

Preliminary tests showed that the upstream portion of the original duct lip had flow separation at velocities of about 30 knots and duct angles of about 70° to 80° as evidenced by tufts on the duct lip, a loud rushing noise, and a sudden change in forces and moments. To overcome this low Reynolds number characteristic of the small-scale model, the radius of the leading portion of the duct lip was increased to 2.5 inches (8 inches, full scale). Further investigation showed that a somewhat smaller lip modification (3 inches, full scale, (fig. 5)) also eliminated the lip stall. Consequently, tests simulating the assumed full-scale airplane were made with the 3-inch (full-scale) duct-lip modification.

Pitching-Moment Characteristics

In general, the wing-tip ducted-fan configuration experienced large nose-up pitching moments at translational velocities and large duct angles (fig. 6), primarily as a result of the large lift produced on the forward lip of the duct in turning the airstream downward through the duct. Note on figure 13 that for the assumed airplane the maximum pitching moment (3,000 foot-pounds) for steady level-flight transition occurs at a speed of about 40 knots and a duct angle of about 70°. Also note that accelerating flight reduces the nose-up pitching moment (figs. 8 and 13) whereas decelerating flight increases the pitching moment (figs. 9 and 13). The variation in moment under accelerating conditions is caused by the thrust acting about the airplane center of gravity (which is below the duct center line) and by changes in flow through the duct. The decelerating flight condition is the most critical from the standpoint of large nose-up moments, in that the change in thrust moment arm adds a nose-up increment and the airstream is turned through a larger angle ($\delta = 90^\circ$ to 100°). The large moments shown for the decelerating condition (fig. 13) would have been even larger if duct stall had not occurred as indicated in figure 9 by some reduction in pitching moment as the angle of attack was increased. Figure 14 shows that the pitching-moment data from the present small-scale investigation with the modified lip agree well with data on a corresponding full-scale configuration (ref. 2); thus, small-scale tests can be used as long as the lip stall encountered at low Reynolds number is avoided. The data of reference 5 for the duct-propeller moment breakdown show the pitching moment of the propeller to be small and the duct contribution to be large.

L
1
5
6
5

The coefficient data at low duct angles (fig. 7) show the wing-duct combination to have an instability similar to that experienced by conventional straight-wing configurations with the horizontal tail removed. Note that the duct increases the instability.

Effective Aspect Ratio

The theory of reference 7 and the experimental data of reference 8 indicate that the effective aspect ratio of an isolated ring airfoil is twice the geometric aspect ratio. Since the effective aspect ratios of a wing alone and duct (ring wing) alone are different, it is of interest to know the effective aspect ratio of a combined configuration (a wing with ring airfoils mounted at each tip, $\delta_{duct} = 0$).

The power-off data of figure 7 can be used to determine the effective aspect ratio of a combined wing-duct configuration (for $\delta = 0$), if it is assumed that the induced drag is given by:

$$C_{D_i} = \frac{C_L^2}{\pi A_e}$$

where A_e is the effective aspect ratio. With the duct removed, the effective aspect ratio A_e is 2.1 which is 78 percent of the geometric aspect ratio ($A_g = 2.67$). With the duct on, the effective aspect ratio A_e is 5.15 based on the wing area used in reducing the data to coefficient form. This is somewhat fictitious, however, because the planform area of the duct, which is also lifting, has been neglected. When the coefficients are based on the total area of the wing plus the projected planform area of the ducts, the effective aspect ratio A_e is 4.02 which is 76 percent of the geometric aspect ratio of the wing plus duct based on the extremity of the duct.

L
1
5
6
5

Comparison of the ratios of effective aspect ratio to the geometric aspect ratio for the plain wing $\left(\frac{A_e}{A_g} = 0.78\right)$ to that for the wing-tip-mounted duct configuration $\left(\frac{A_e}{A_g} = 0.76\right)$ shows that for most practical purposes the induced drag of a wing-tip ducted-fan configuration is equal to that of a plain wing of similar overall span and area. The effect of the duct probably becomes more important where the duct area is a greater percent of the total area.

Power Required

The basic data of figure 6 show the power to be essentially invariant with angle of attack but show changes in power with duct angle and speed. Figure 13 shows the expected reduction of horsepower with speed for steady level-flight equilibrium conditions.

The horsepower required in hovering is less than that obtained on the full-scale airplane (ref. 3) or on the full-scale wind-tunnel model (fig. 16 and ref. 2), primarily because the model duct is much cleaner internally (smaller number of duct supports, no straightening vanes or inlet guide vanes, smaller number of propeller blades, and so forth) than the full-scale duct. Under level-flight accelerating conditions (fig. 13, 0.313g), the power required through the transition speed range increases to about the same level as that required to hover. For decelerating flight of 0.313g, the power required is about the same as that experienced for steady level flight. This is probably a result of the lift component of the thrust vector being essentially equal to the thrust when decelerating. In addition there is a decelerating force

caused by a larger profile drag of the duct when operating at high angles and forward speed and some drag increase due to stall when decelerating.

Figure 15 shows that flying the wing-tip ducted-fan configuration with a wing angle of attack of 15° reduces the power required considerably (about 30-percent reduction at 50 knots) because the load is more nearly uniformly distributed over the span and thus reduces the induced drag and power. At zero angle of attack with essentially zero wing lift, the configuration is essentially flying on the two ducts which are surfaces of very low aspect ratio and which have high induced drag.

L
1
5
6
5

The propeller-duct static thrust efficiency in hovering computed by using the equation

$$\eta_s = \frac{T^{3/2}}{1,100P\sqrt{\rho A_E}}$$

was found to be about 81 percent. This value is somewhat higher than expected, probably because of the cleanliness of the duct-propeller combination (no turning vanes, etc.; see fig. 3). Note that the static efficiency is based on the exit area.

Root Bending Moments

Root bending moments caused by normal and axial forces on the semispan wing-duct configuration are presented in figure 6(b). These data have been used to determine the lateral center of pressure of the normal force for the wing-duct combination at angles of attack of -1° and 15°. (See fig. 15.) These curves show that the center of pressure for the hovering case is at the center of the duct (about 81 percent of the span to the outer duct rim) as would be expected. As forward speed is increased to speeds above the normal power-off stalling speed, the center of pressure moves inboard to about 60 percent of the wing-duct span when the wing is operating at low lift ($\alpha = -1^\circ$), that is, flying largely on duct lift. For the condition where the wing carries an increasing percentage of the lift ($\alpha = 15^\circ$), the center of pressure moves inboard to about the 42-percent wing-duct-span position.

Exit Vanes

In an attempt to control the large nose-up moments, vanes (fig. 5) were placed in the exit of the basic duct to deflect the flow downward and thus produce a negative moment. The results show that large nose-down trim moments can be obtained with duct-exit control vanes (fig. 10), although there is a power penalty. Similar results (full scale) were

obtained in reference 2. It should be noted that the vanes were not designed for this model but were made from available cambered airfoil stock and probably required more power than would specially designed vanes.

Ground Effect

Figure 16 shows that for steady level flight the nose-up pitching moments and the horsepower are reduced as the ground is approached at transition speeds. As the speed is reduced to hovering, the horsepower required is increased when in the presence of the ground. The data presented in reference 6 show this condition can occur depending upon the blade angle of the shrouded propeller.

L
1
5
6
5

The reduction in horsepower at transition speeds can be attributed in part to the lower induced drag of the complete configuration when in ground effect (fig. 7(a)). It is felt that the increase in horsepower near hovering is caused by alterations in the flow field around the configuration and through the duct, possibly including back pressure effects on the propeller, and suction effects on the wing lower surface. (See ref. 6.)

Effect of Duct-Lip Stall and Model Tests

Figure 11 shows the effect of duct-lip stall at critical duct angles of 60° to 80° and speeds of 30 to 60 knots. Note that for low duct angles there is no apparent indication of duct-lip stall; therefore, the original duct gives reliable data for the low duct angles. The degree of lip stall is illustrated in figures 12 and 17 by the curves for different lip modifications. These data also show why, in model testing, extreme care must be exercised in preventing duct-lip stall on small-scale wind-tunnel models if full-scale results are to be simulated.

Comparison of these results (stalled and unstalled data) also shows the problems to be expected on a full-scale ducted-fan configuration if duct-lip stall should occur. Note (fig. 11) that large angles of attack can be obtained before lip stall (flow separation) occurs; however, once lip stall occurs, the lift and moment do not return to the same level upon reducing the angle of attack because of hysteresis of the flow reattachment. The hysteresis of flow reattachment could possibly present a dynamic stability problem on a full-scale airplane.

The data show that lip-stall effects on pitching moment are more pronounced when in ground effect. (Compare figs. 12(a) and 12(b).) There is no appreciable effect of stall on power when in ground effect.

The effects of duct-lip stall out of ground effect appear as a large increase in power required, in addition to large changes in pitching moments. (See fig. 17.)

These data in general illustrate the moment and power problem which would be encountered on full-scale aircraft if duct-lip stall should occur in the critical transition speed range.

Dynamic-Pressure Ratios and Downwash Angles

L
1
5
6
5

Dynamic-pressure ratios and downwash angles were obtained for the configuration with the original duct (no lip modification) for several acceleration and ground height conditions. (See figs. 18 to 21.) It is believed that the dynamic pressure and downwash ratios would not be affected appreciably by the duct-lip modifications. These data were obtained at fixed vane positions (fig. 4); that is, the tail position would change with change in angle of attack. (See ref. 4 for more vane detail.)

In general, the dynamic pressure at the vanes is equal to the free-stream dynamic pressure $\frac{q}{q_o} = 1.0$ for $\frac{h}{\bar{c}} = \infty$ (see figs. 18 and 19) except where the duct-propeller slipstream impinges on the vanes, usually for the large duct angles. (See figs. 19(a) and 19(b), vane 5.) The effect of duct-propeller slipstream on the dynamic-pressure ratios becomes much greater (for the large duct angles) when in proximity to the ground (see figs. 20 and 21) primarily because the ground deflects the high energy slipstream past some of the vanes. Some extremely large values are obtained at $\frac{h}{\bar{c}} = 0.75$ on vane 4. (See figs. 21(a), 21(b), and 21(c).) Vanes outside the deflected slipstream show that dynamic pressure at the vanes is essentially equal to the free-stream value $\frac{q}{q_o} = 1.0$.

Figure 18 shows the effect of various model components (wing alone, duct, and propeller) on the downwash at zero duct angle. The data of figure 19 (out of ground effect) show some variation in downwash at all vane positions, probably because of the wing. When in ground effect the downwash is essentially zero for vanes immersed in the deflected slipstream, primarily because the slipstream is deflected parallel to the ground. (See fig. 21, vane 4.) The changes in downwash obtained on the full-scale semispan model are shown in references 2 and 5.

CONCLUDING REMARKS

Analysis of wind-tunnel results obtained on a powered semispan ducted-fan model show that large nose-up pitching moments are obtained at transition speeds of about 40 knots and duct angles of about 70°. The nose-up pitching moments are reduced somewhat under accelerating flight conditions but become more severe under decelerating flight conditions. Ground proximity reduces the nose-up moment. The results show that large trim moments can be obtained with duct-exit control vanes.

L
1
5
6
5

The results show that duct-propeller stall reduces the lift and nose-up pitching moment but increases the horsepower required. The results also show that flying the wing-tip ducted-fan configuration at a wing angle of attack of 15° (unloading the duct) reduces the power required about 30 percent at 50 knots. The results in general show full-scale results can be simulated with small-scale models if duct-lip separation effects encountered at low Reynolds numbers are avoided.

Langley Research Center,
National Aeronautics and Space Administration,
Langley Air Force Base, Va., September 7, 1961.

REFERENCES

1. Grunwald, Kalman J., and Goodson, Kenneth W.: Aerodynamic Loads on an Isolated Shrouded-Propeller Configuration for Angles of Attack From -10° to 110°. NASA TN D-995, 1962.

2. Yaggy, Paul F., and Mort, Kenneth W.: A Wind-Tunnel Investigation of a 4-Foot-Diameter Ducted Fan Mounted on the Tip of a Semispan Wing. NASA TN D-776, 1961.

3. Tapscott, Robert J., and Kelley, Henry L.: A Flight Study of the Conversion Maneuver of a Tilt-Duct VTOL Aircraft. NASA TN D-372, 1960.

4. Kuhn, Richard E., and Hayes, William C., Jr.: Wind-Tunnel Investigation of Longitudinal Aerodynamic Characteristics of Three Propeller-Driven VTOL Configurations in the Transition Speed Range, Including Effects of Ground Proximity. NASA TN D-55, 1960.

5. Yaggy, Paul F., and Goodson, Kenneth W.: Aerodynamics of a Tilting Ducted Fan Configuration. NASA TN D-785, 1961.

6. Schade, Robert O.: Ground Interference Effects. NASA TN D-727, 1961.

7. Ribner, Herbert S.: The Ring Airfoil in Nonaxial Flow. Jour. Aero. Sci., vol. 14, no. 9, Sept. 1947, pp. 529-530.

8. Fletcher, Herman S.: Experimental Investigation of Lift, Drag, and Pitching Moment of Five Annular Airfoils. NACA TN 4117, 1957.

L
1
5
6
5

TABLE I.- DUCT COORDINATES

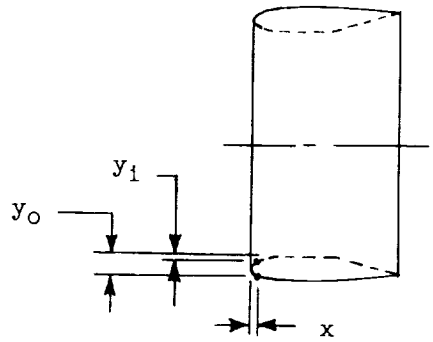

x, in.	y_i, in.	y_o, in.
0	0.875	0.875
.078	.663	1.144
.125	.589	1.206
.188	.513	1.256
.250	.463	1.287
.312	.406	1.325
.438	.337	1.375
.625	.263	1.437
.938	.163	1.506
1.250	.100	1.556
1.562	.050	1.587
1.875	.019	1.613
2.188	.006	1.625
2.500	0	1.637
2.812	0	1.644
Straight line	0	1.644
↓	0	1.644
	0	1.644
	0	1.644
	0	1.644
5.375	0	1.644
5.938	Straight line	1.625
6.250	↓	1.600
6.562		1.575
6.875		1.537
7.188		1.500
7.500		1.463
7.812		1.425
8.125		1.375
8.438		1.331
8.750		1.281
9.375		1.163
10.312	.950	.981

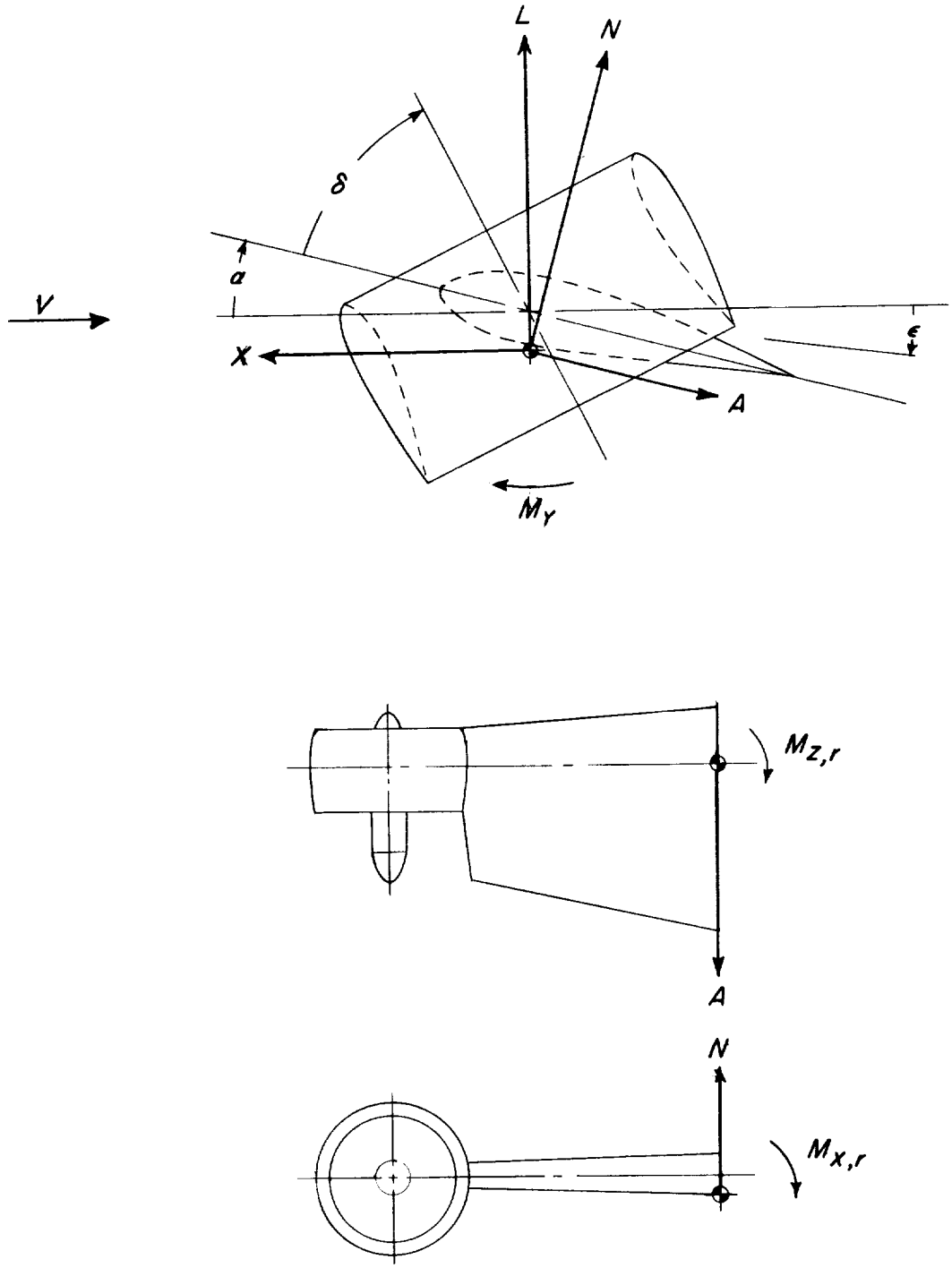

Figure 1.- Axis system showing positive sense of forces, moments, and angles.

L-1565

L-1565

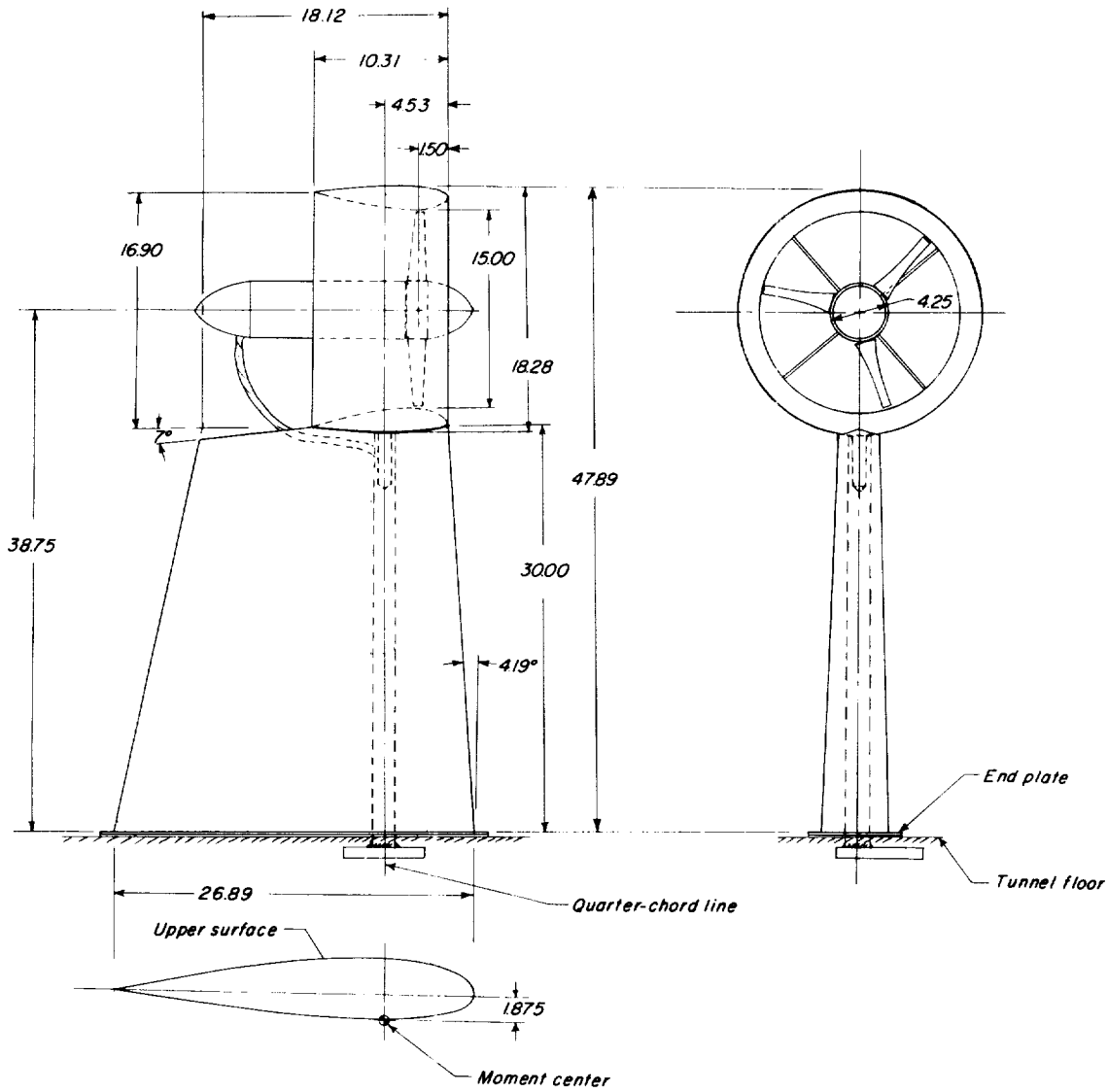

Figure 2.- Geometric characteristics of the semispan wind-tunnel model. All dimensions are in inches.

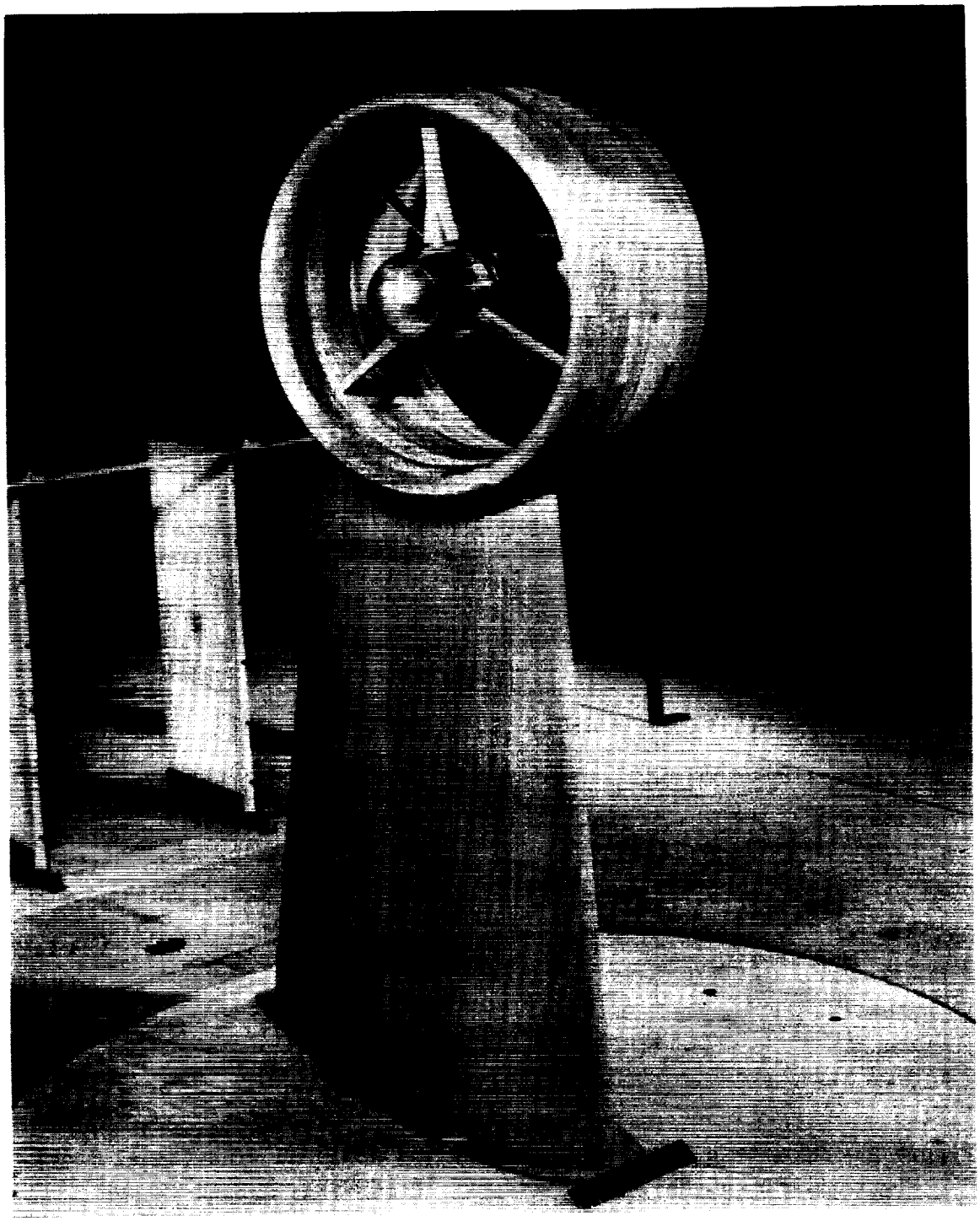

L-59-2628

Figure 3.- Photograph of the ducted-fan semispan model.

L-1565

L-1565

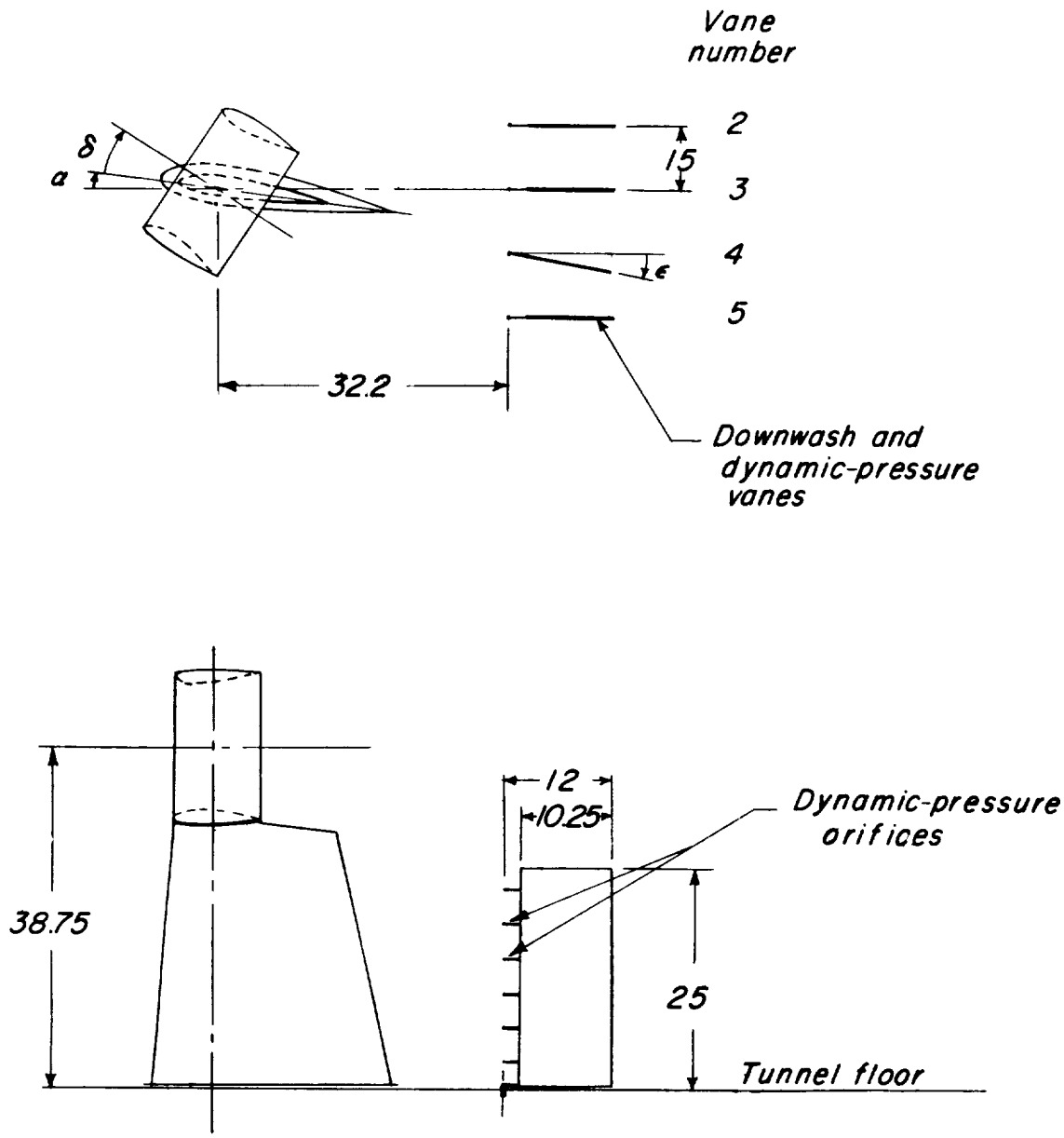

Figure 4.- Downwash vane locations. Dimensions are in inches.

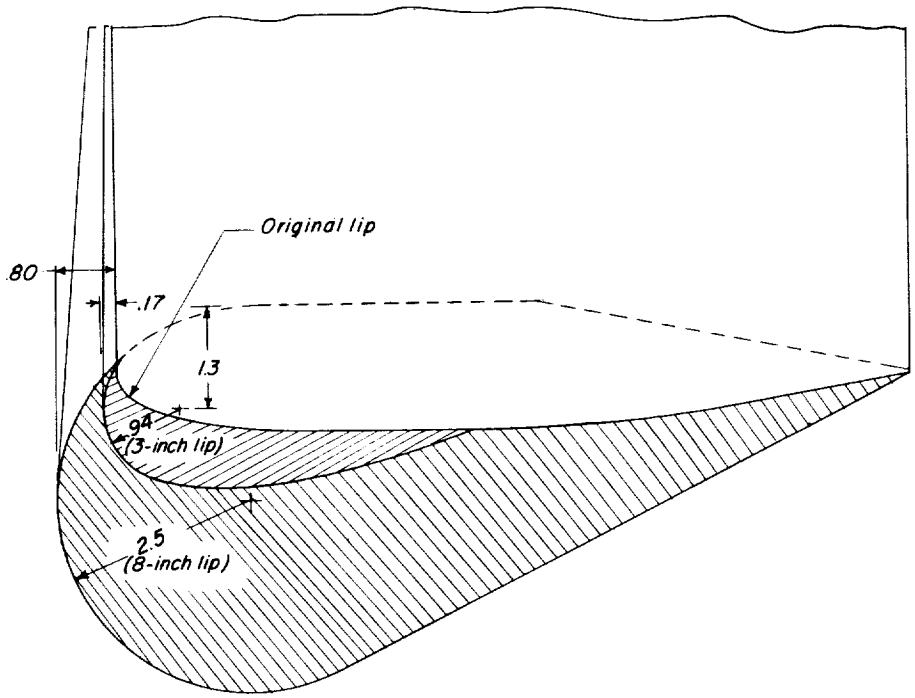

Duct-lip modifications

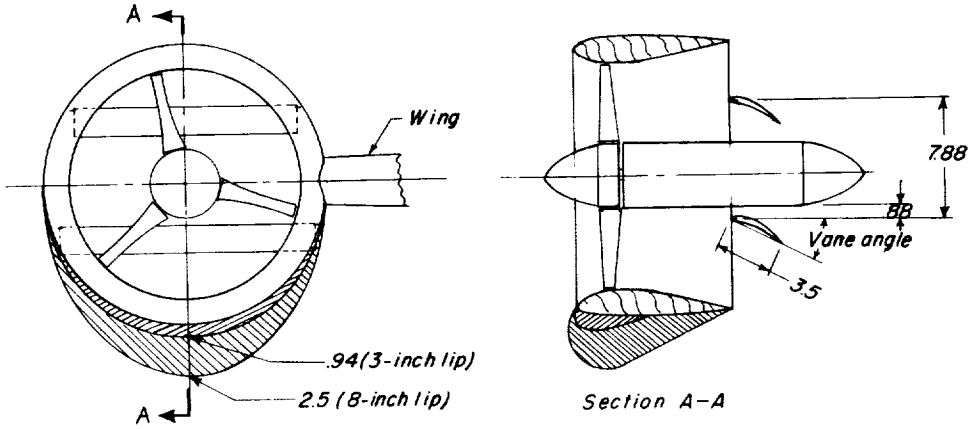

Exit vanes

Figure 5.- Duct-lip modifications and exit vanes.

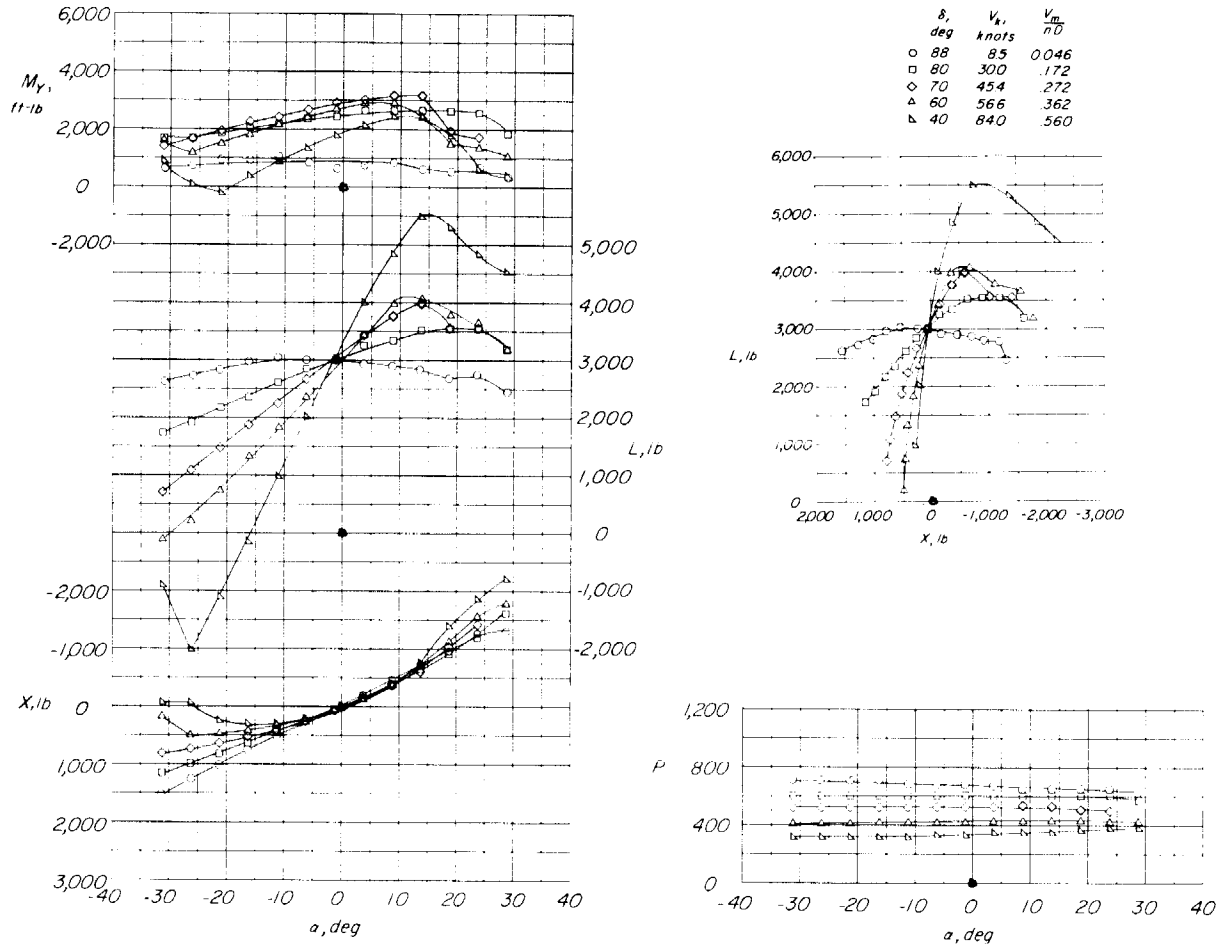

(a) Longitudinal characteristics.

Figure 6.- Aerodynamic characteristics of model with 3-inch duct-lip modification. $(0g)_{\alpha=0}$ steady level-flight condition; $\frac{h}{\bar{c}} = \infty$.

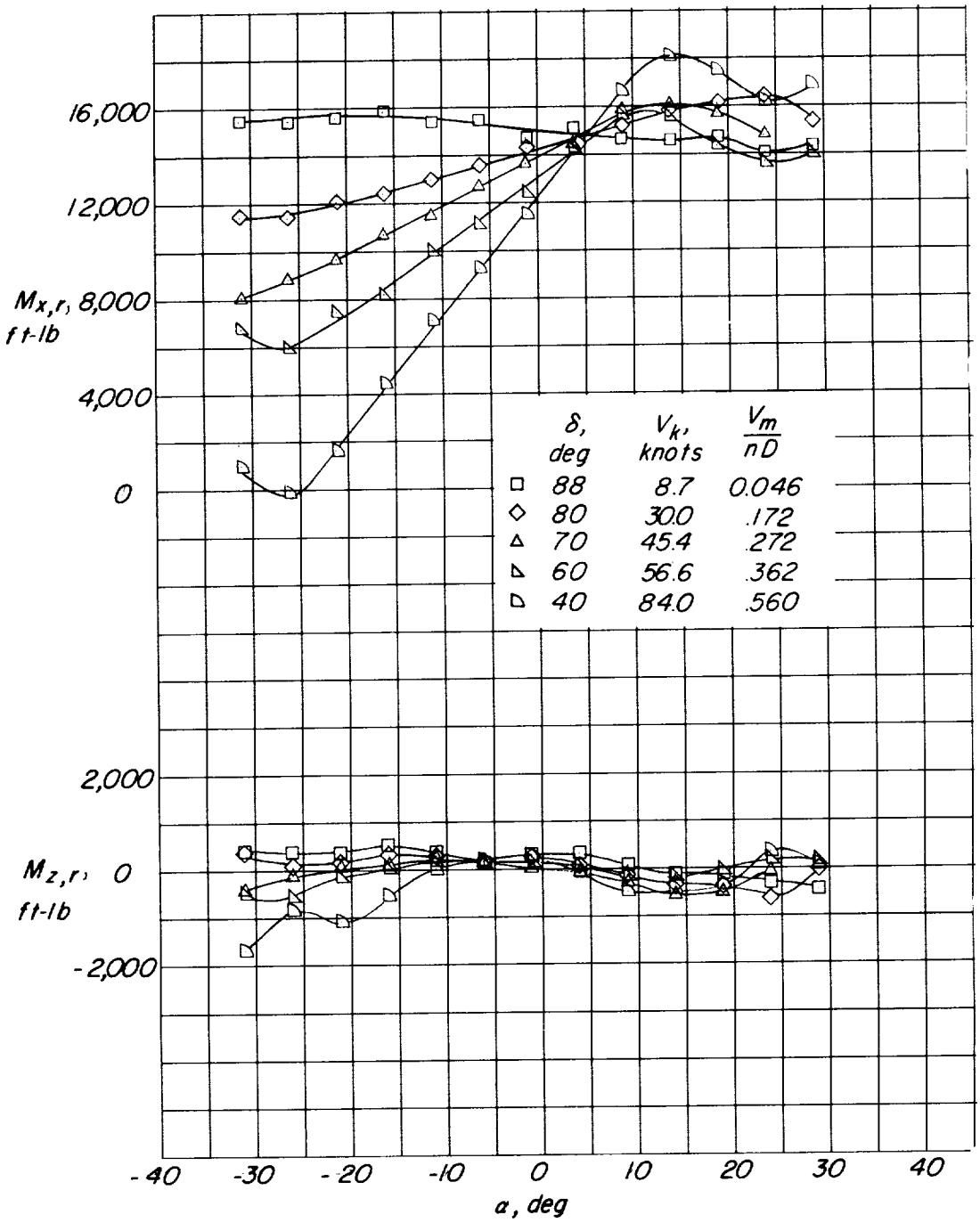

(b) Root bending moments.

Figure 6.- Concluded.

L-1565

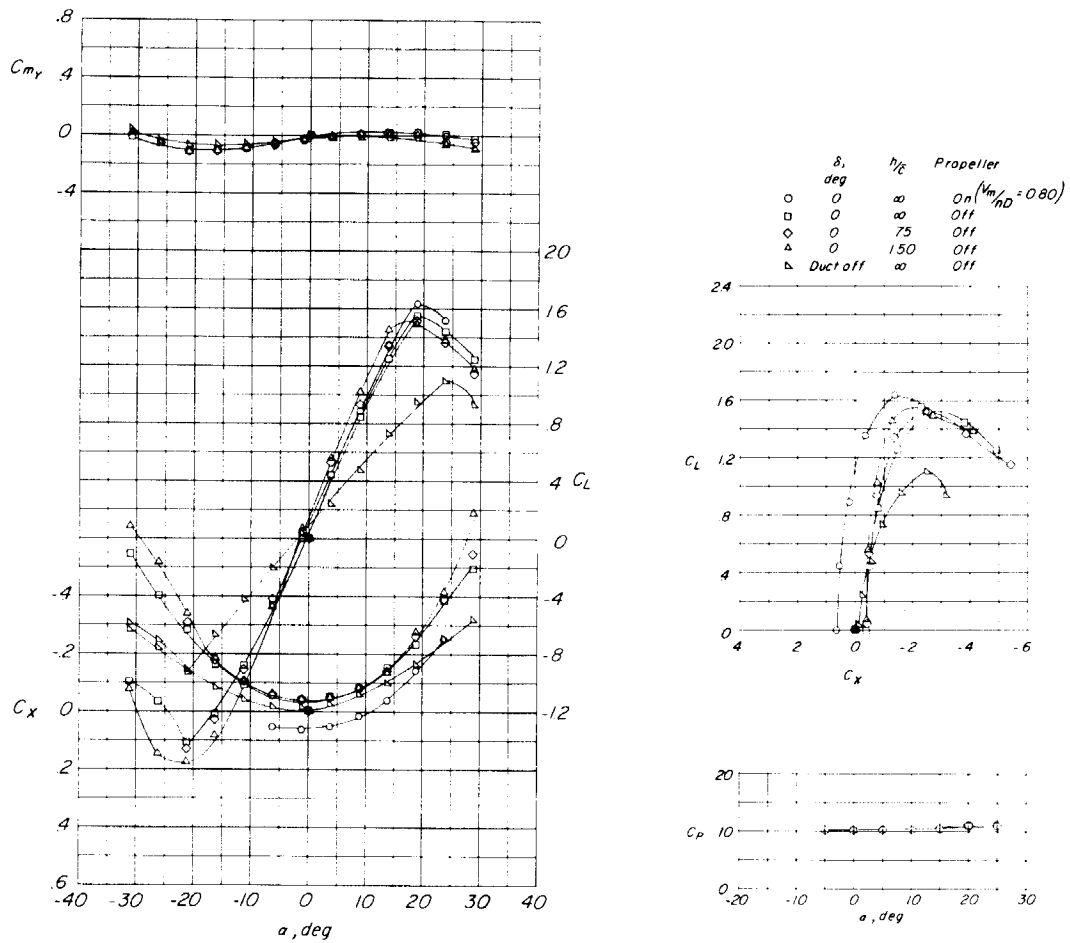

(a) $\delta = 0^{\circ}$.

Figure 7.- Aerodynamic coefficient characteristics of model at low duct angles with the original duct. $\beta = 24^{\circ}$.

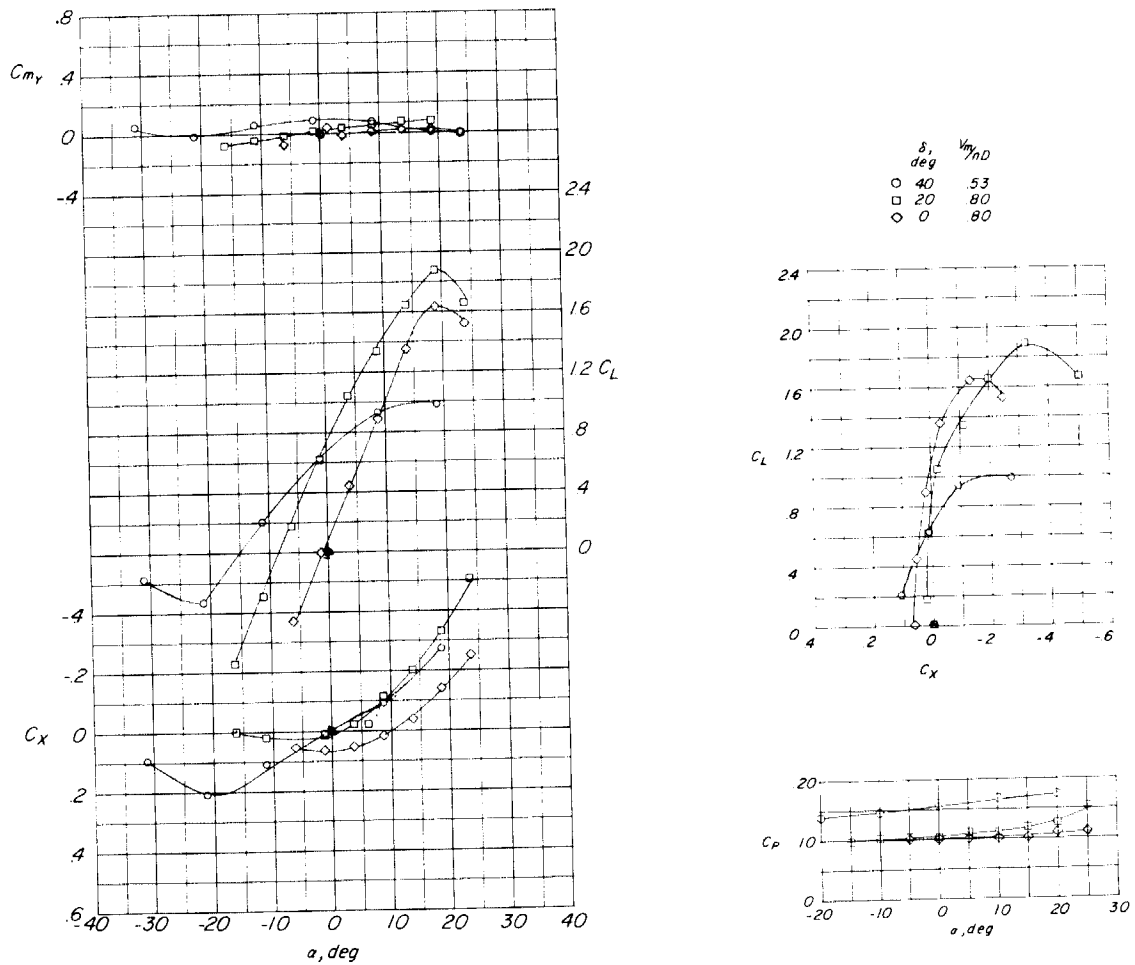

(b) $\delta = 0^{\circ}$, 20°, and 40°; $\frac{h}{\bar{c}} = \infty$.

Figure 7.- Concluded.

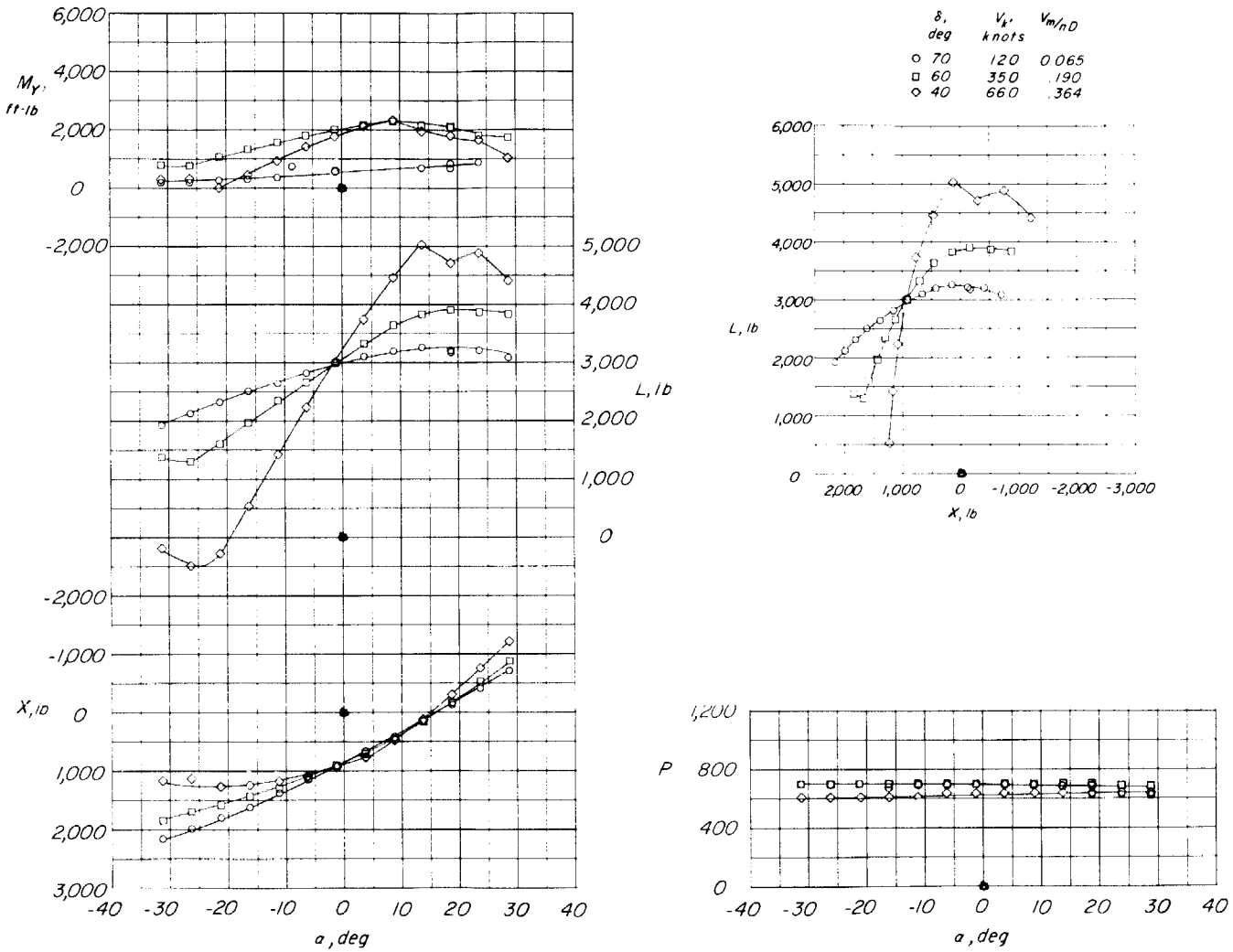

Figure 8.- Aerodynamic characteristics of model with 3-inch duct-lip modification. $(0.313g)_{\alpha=0}$ accelerating flight condition; $\frac{h}{\bar{c}} = \infty$.

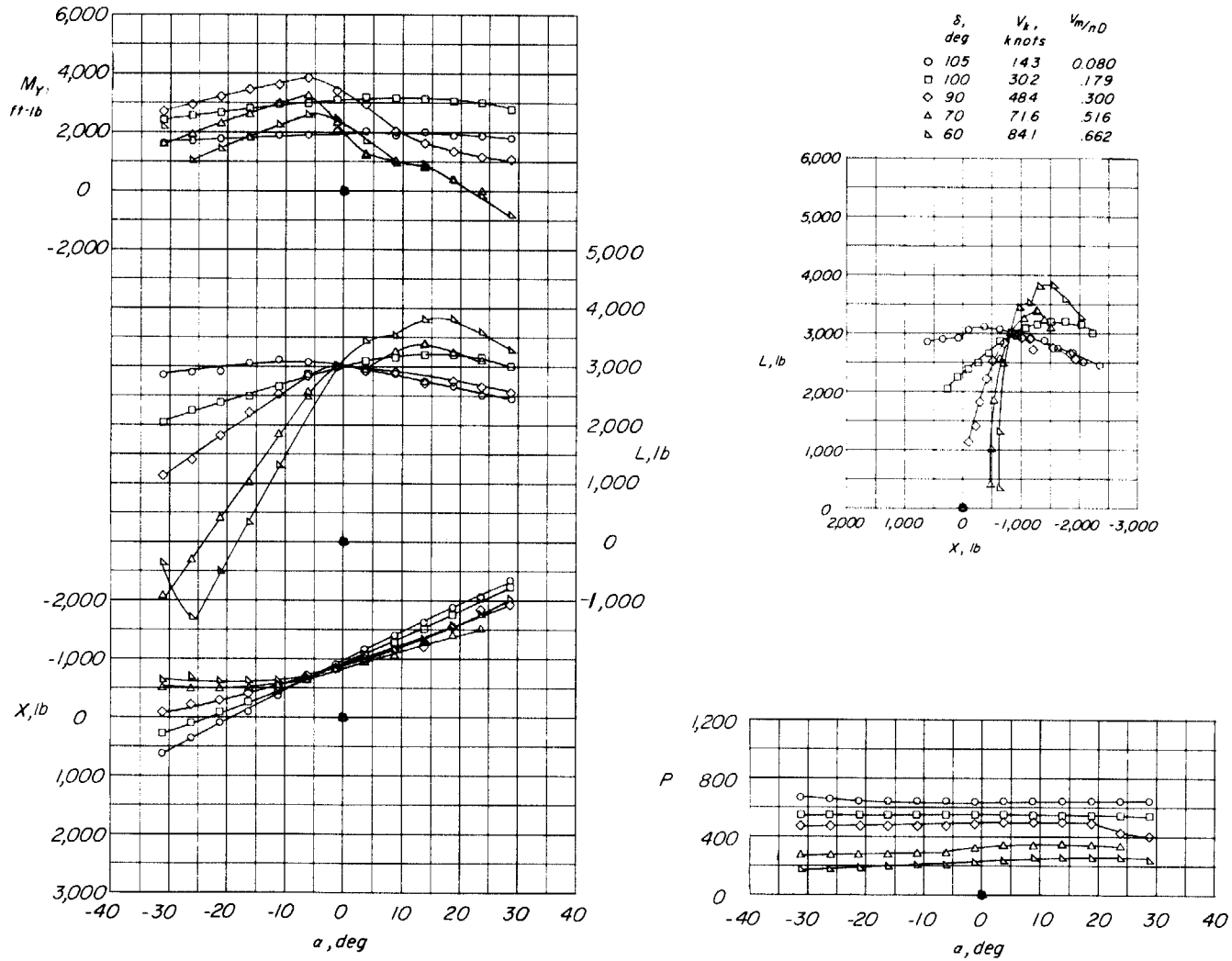

Figure 9.- Aerodynamic characteristics of model with 3-inch duct-lip modification. $(0.313g)_{\alpha=0}$ decelerating flight condition; $\frac{h}{\bar{c}} = \infty$.

L-1565

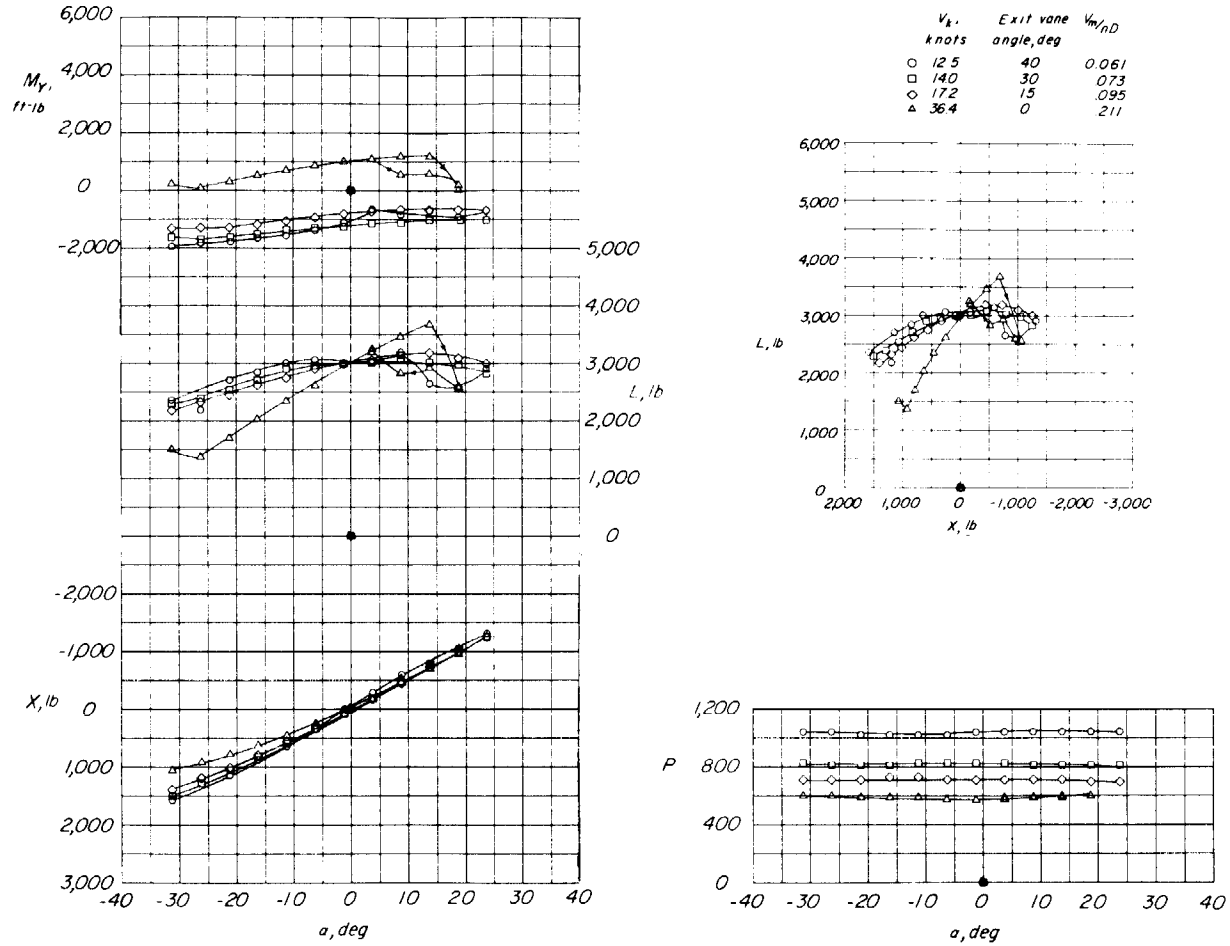

Figure 10.- Effect of duct exit vane deflection on the aerodynamic characteristics of a wing-tip ducted-fan configuration. Original duct, $(Og)_{\alpha=0}$, steady level-flight condition; $\frac{h}{\bar{c}} = \infty$; $\delta = 60^{\circ}$.

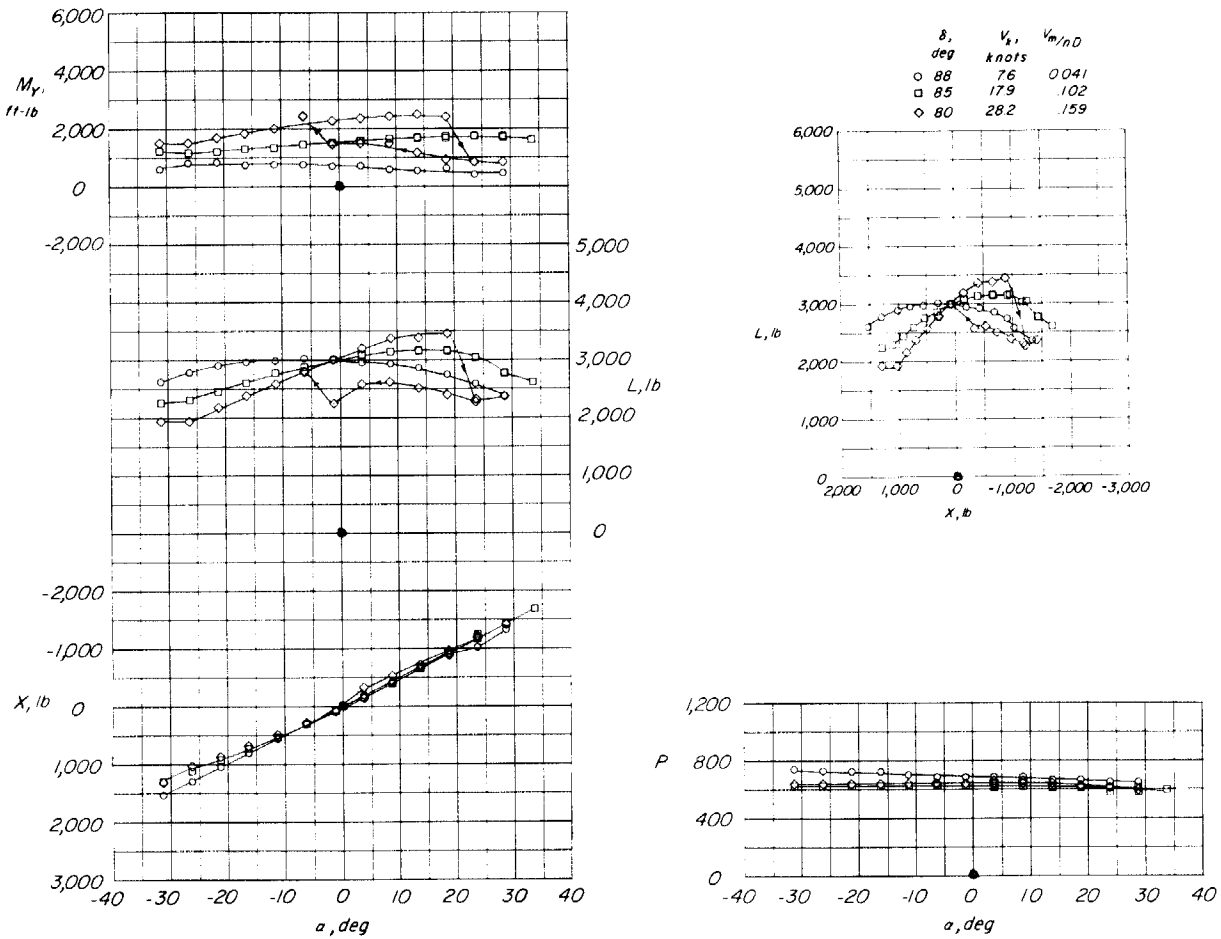

(a) $\delta = 88^\circ$, 85°, and 80°.

Figure 11.- Aerodynamic characteristics of model with original duct. $(Og)_{\alpha=0}$ steady level-flight condition; $\frac{h}{\bar{c}} = \infty$.

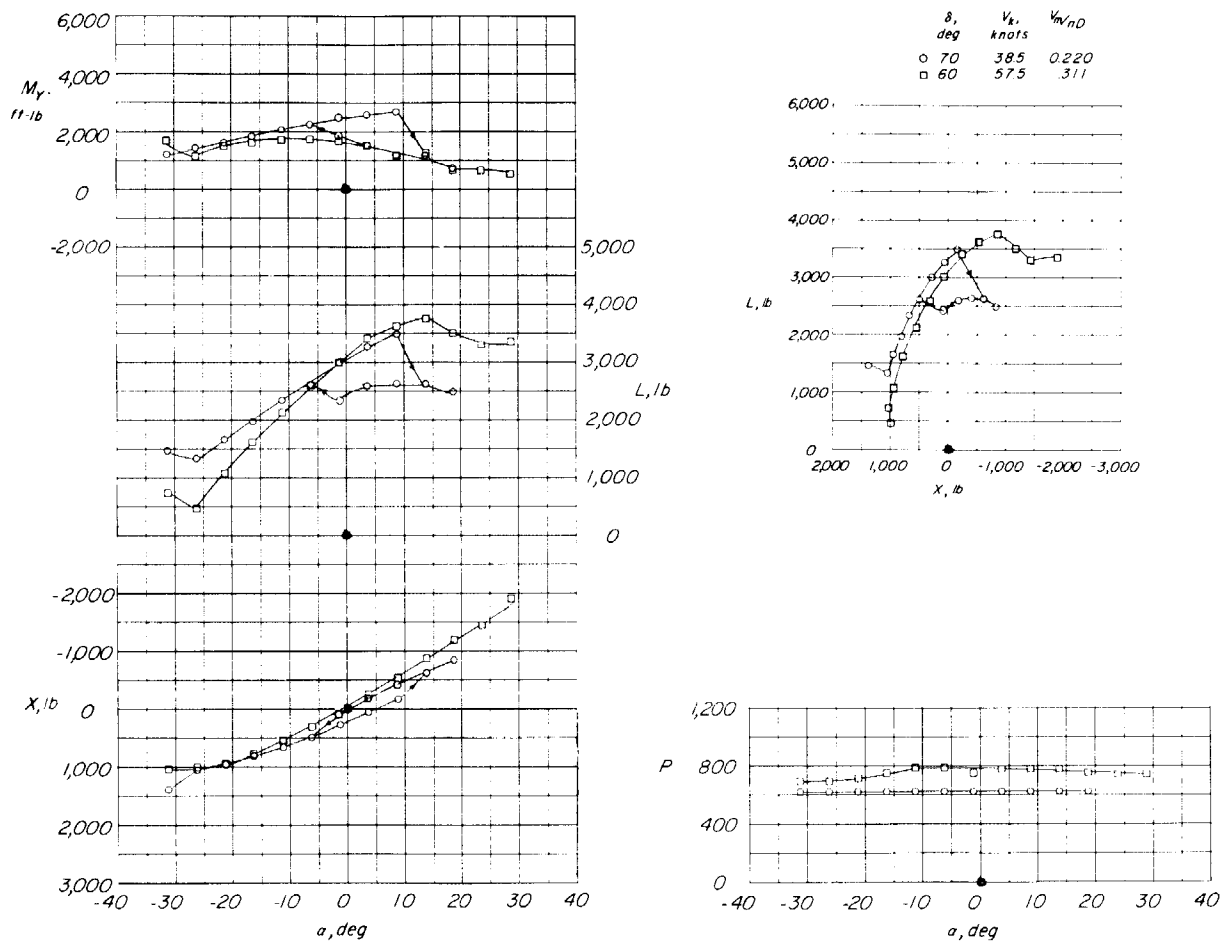

(b) δ = 70° and 60°.

Figure 11.- Concluded.

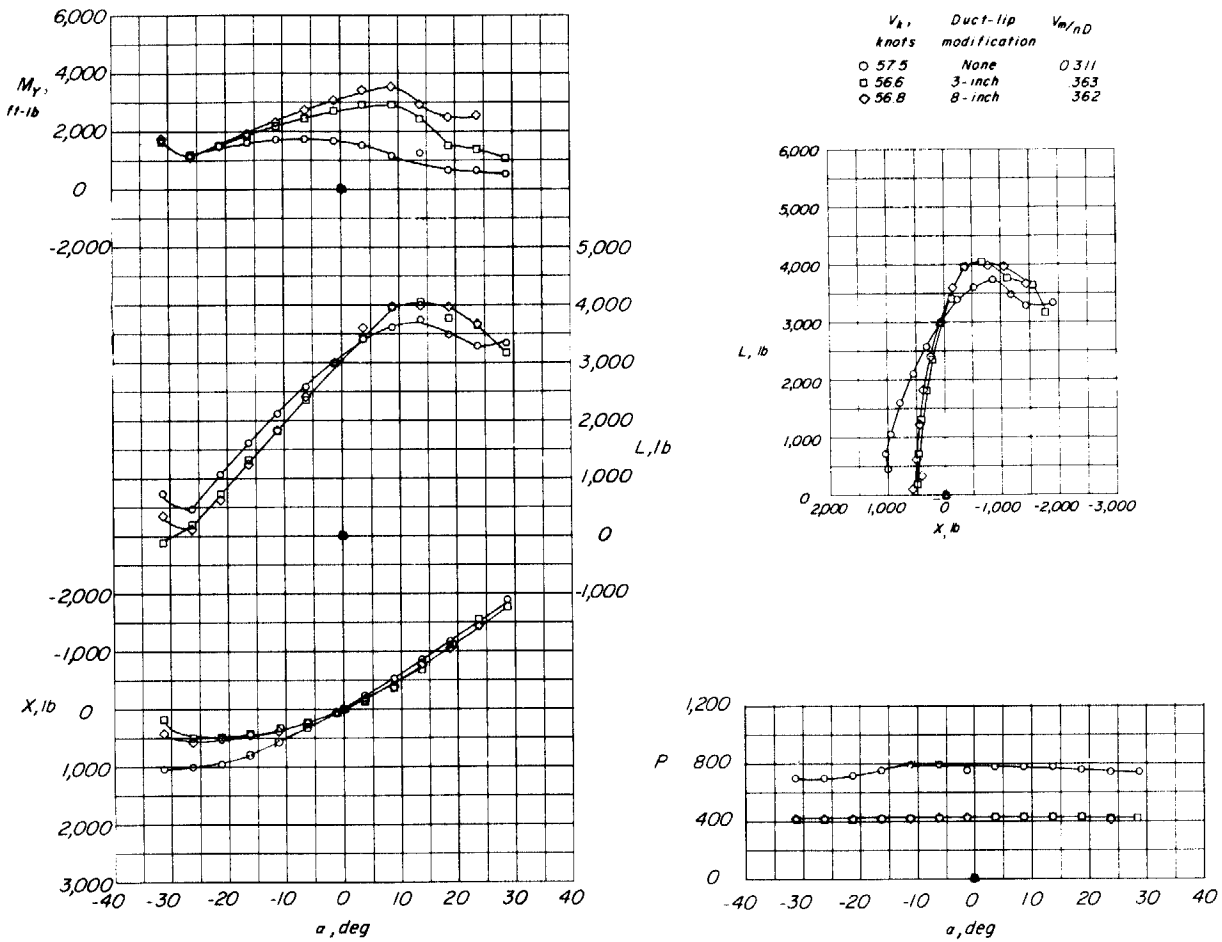

(a) $\frac{h}{\bar{c}} = \infty$.

Figure 12.- Effect of duct-lip modification and duct exit vanes on the aerodynamic characteristics of a wing-tip ducted-fan configuration. $(0g)_{\alpha=0}$ steady level-flight condition; $\delta = 60^{\circ}$.

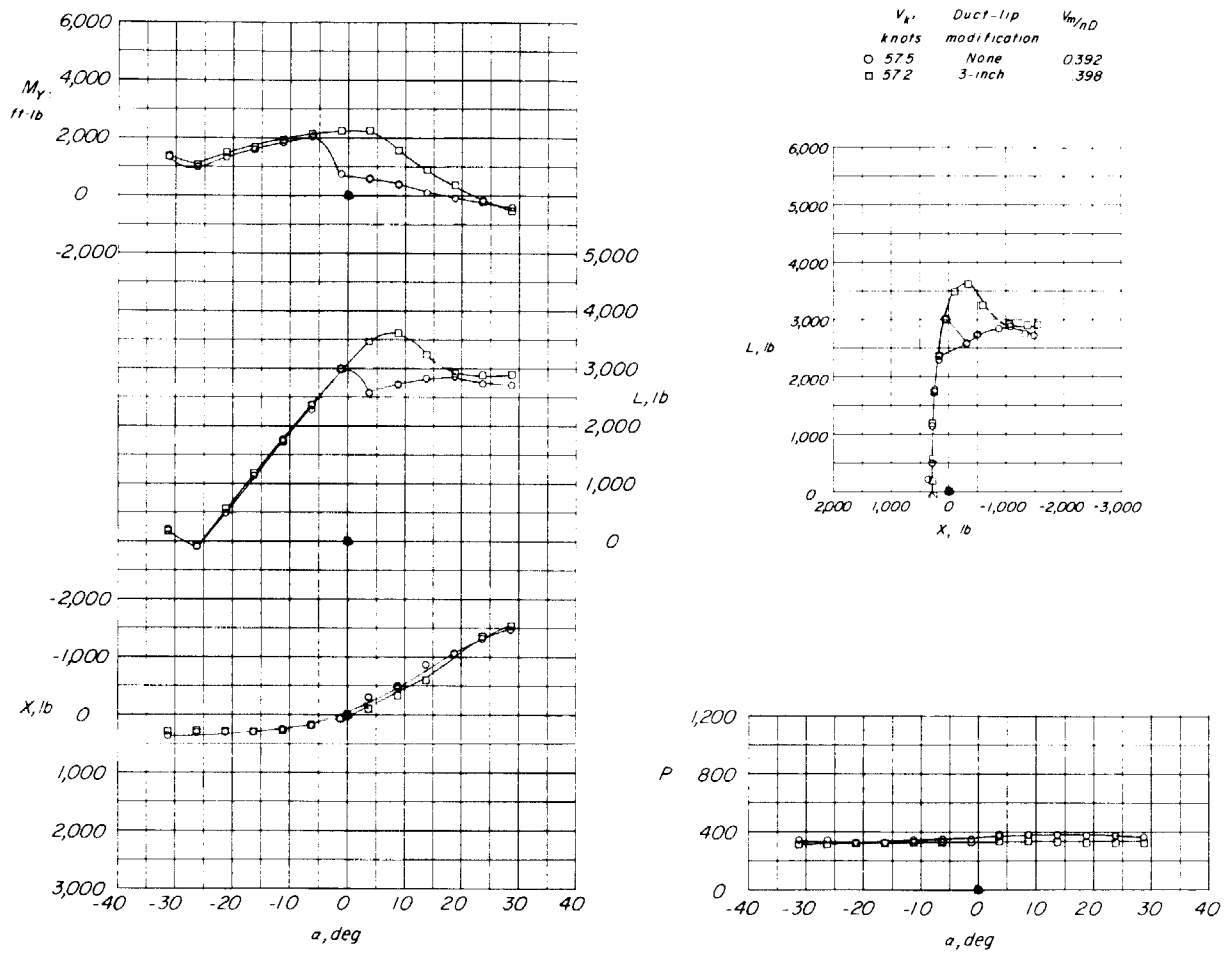

(b) $\frac{h}{c} = 0.75$.

Figure 12.- Concluded.

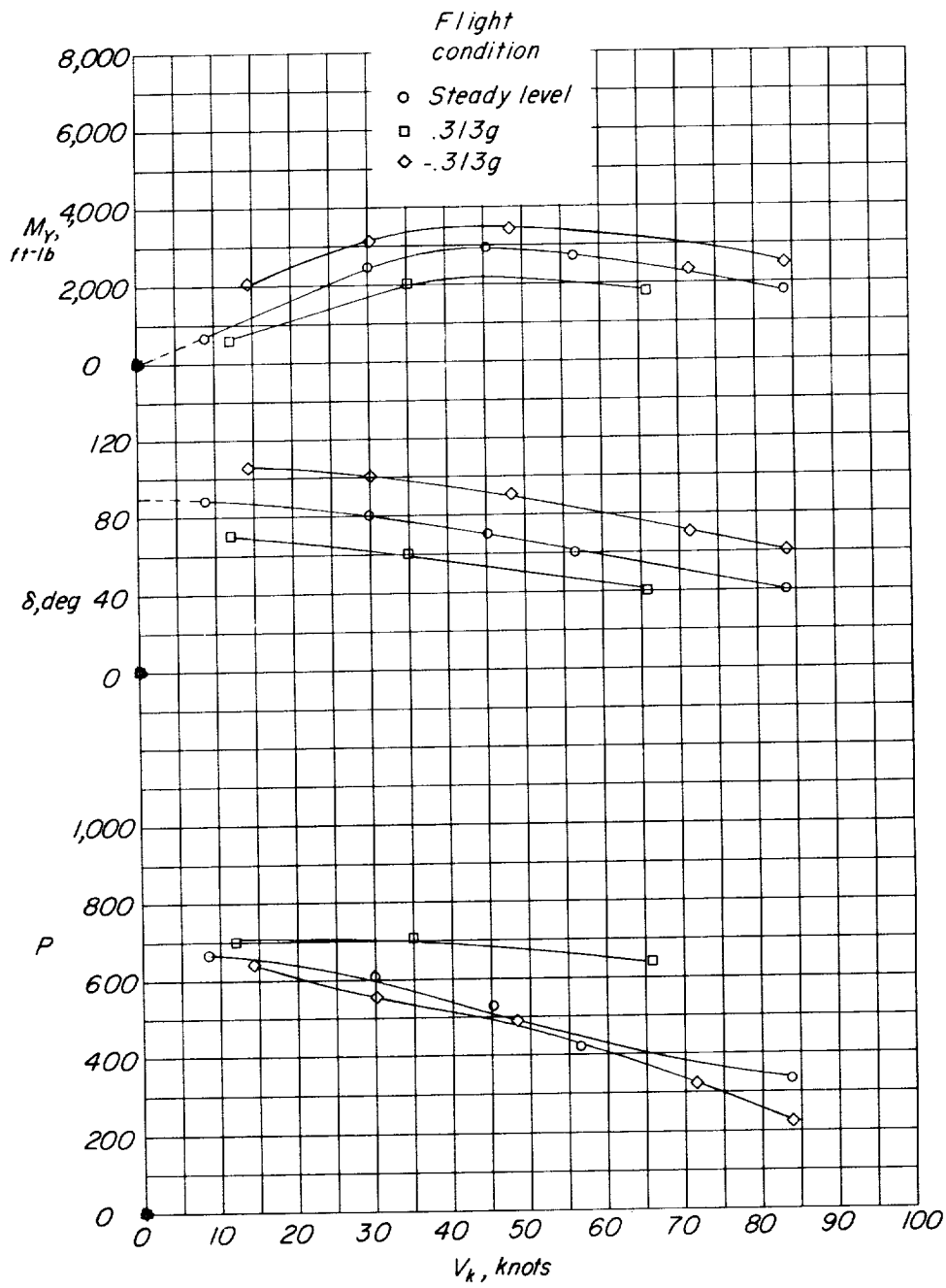

Figure 13.- Effect of flight condition (acceleration) on the power required, duct angle, and pitching moment of a wing-tip ducted-fan configuration through a speed range. 3-inch duct-lip modification; $\frac{h}{\bar{c}} = \infty$.

L-1565

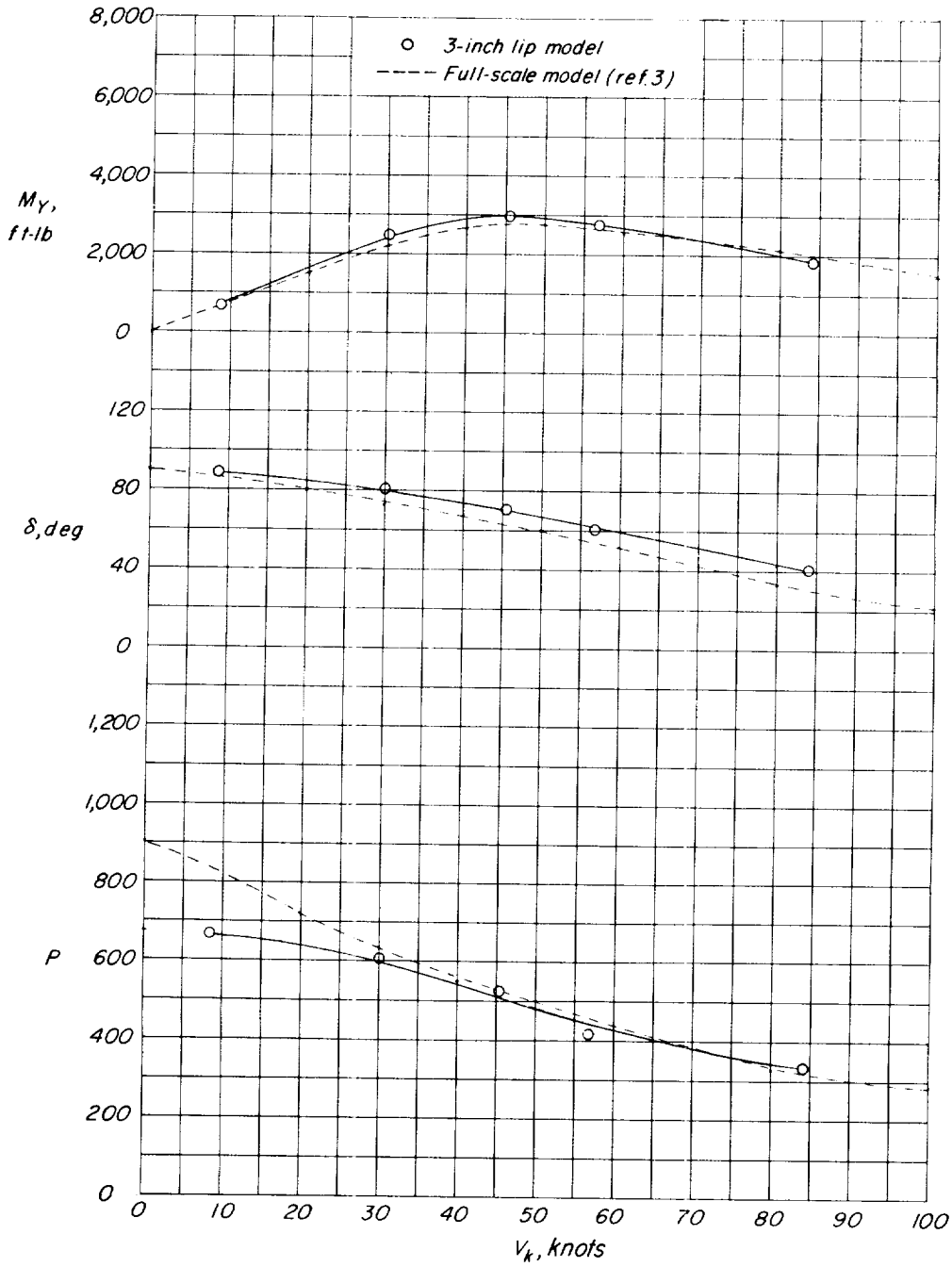

Figure 14.- Comparison of model and full-scale power required, duct angle, and pitching moment of a wing-tip ducted-fan configuration. $(Og)_{\alpha=0}$ steady level-flight condition; $\frac{h}{\bar{c}} = \infty$.

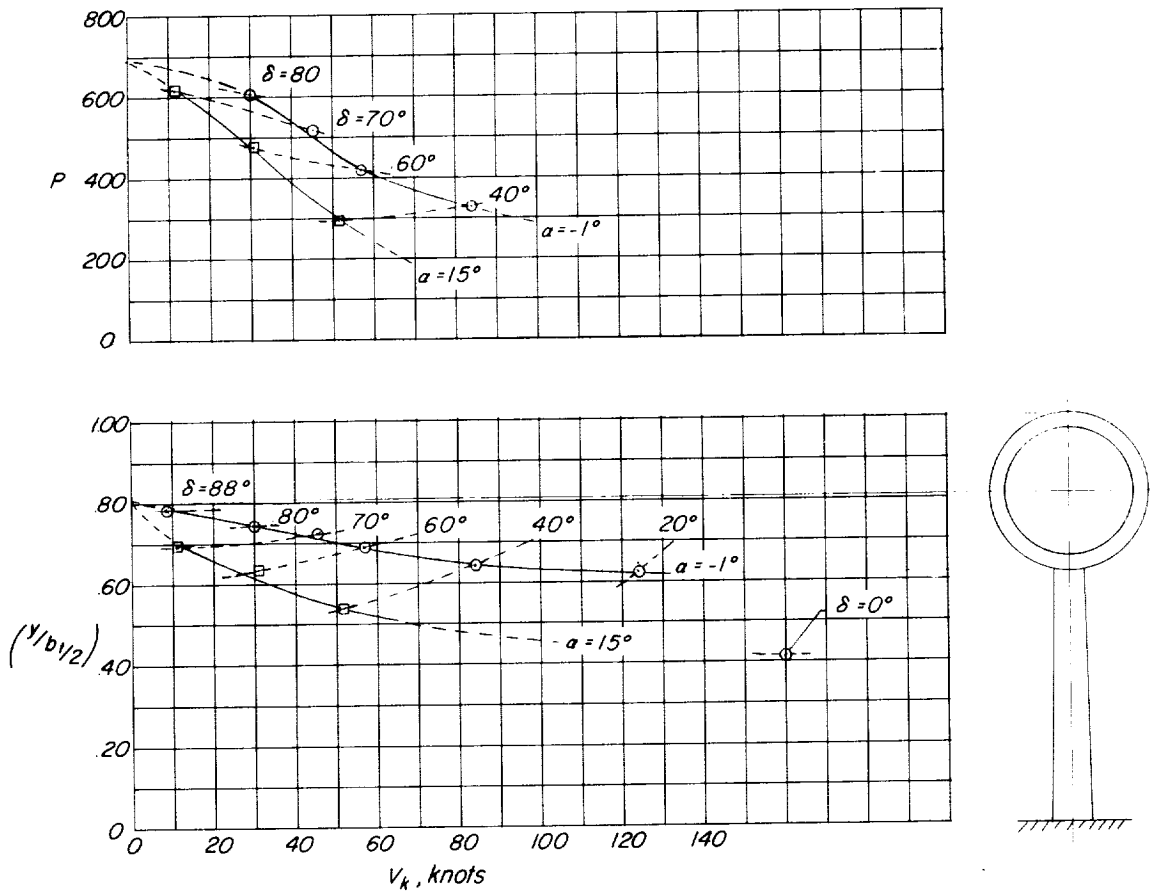

Figure 15.- Effect of angle of attack on spanwise center of pressure and horsepower variation with speed. 3-inch duct-lip modification; $\frac{h}{c} = \infty$; $(Og)_{\alpha=0}$ steady level flight.

L-1565

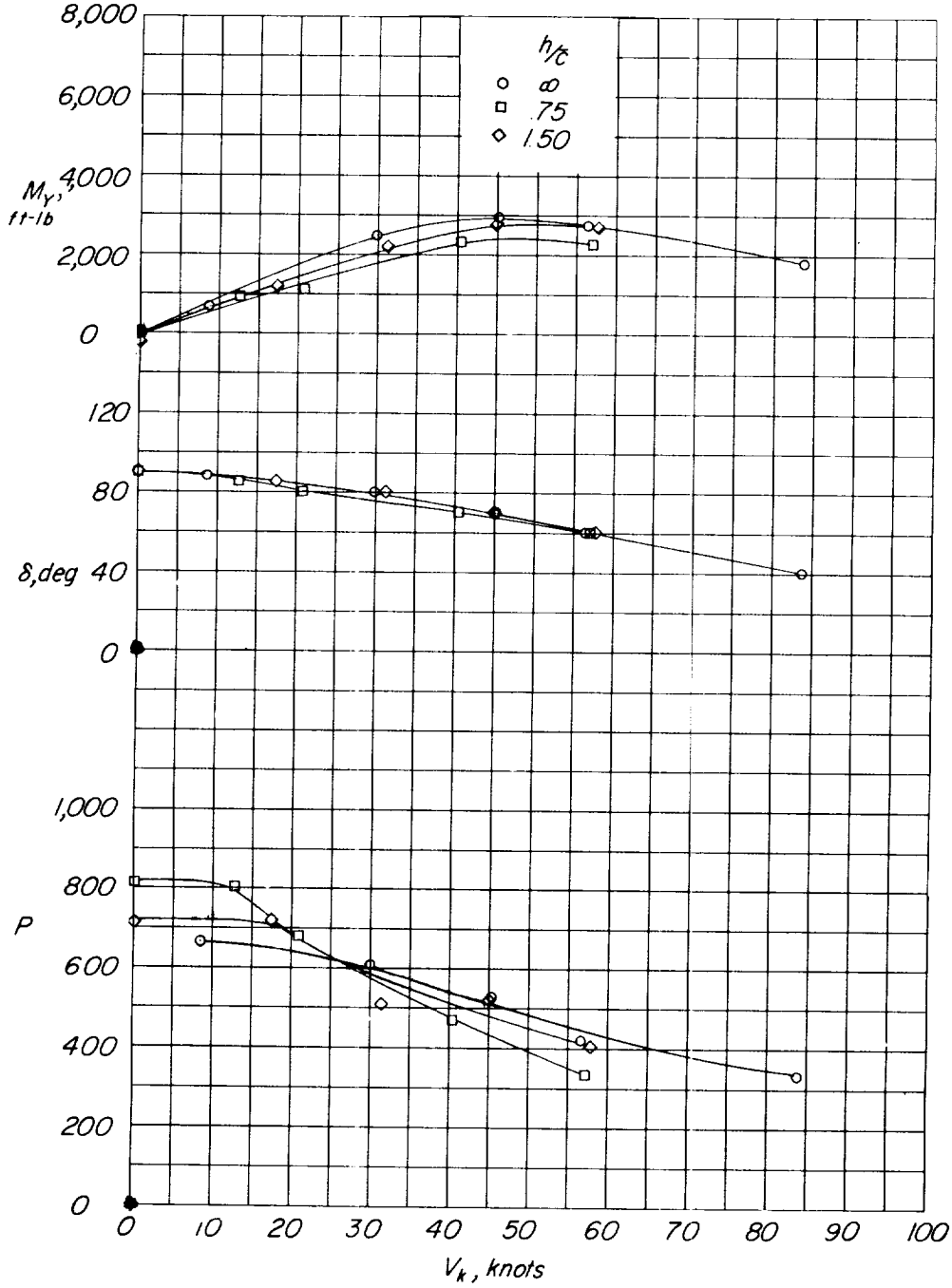

Figure 16.- Effect of ground proximity on the power required, duct angle, and pitching moment of a wing-tip ducted-fan configuration through a speed range. 3-inch duct-lip modification. $(0g)_{\alpha=0}$ steady level flight.

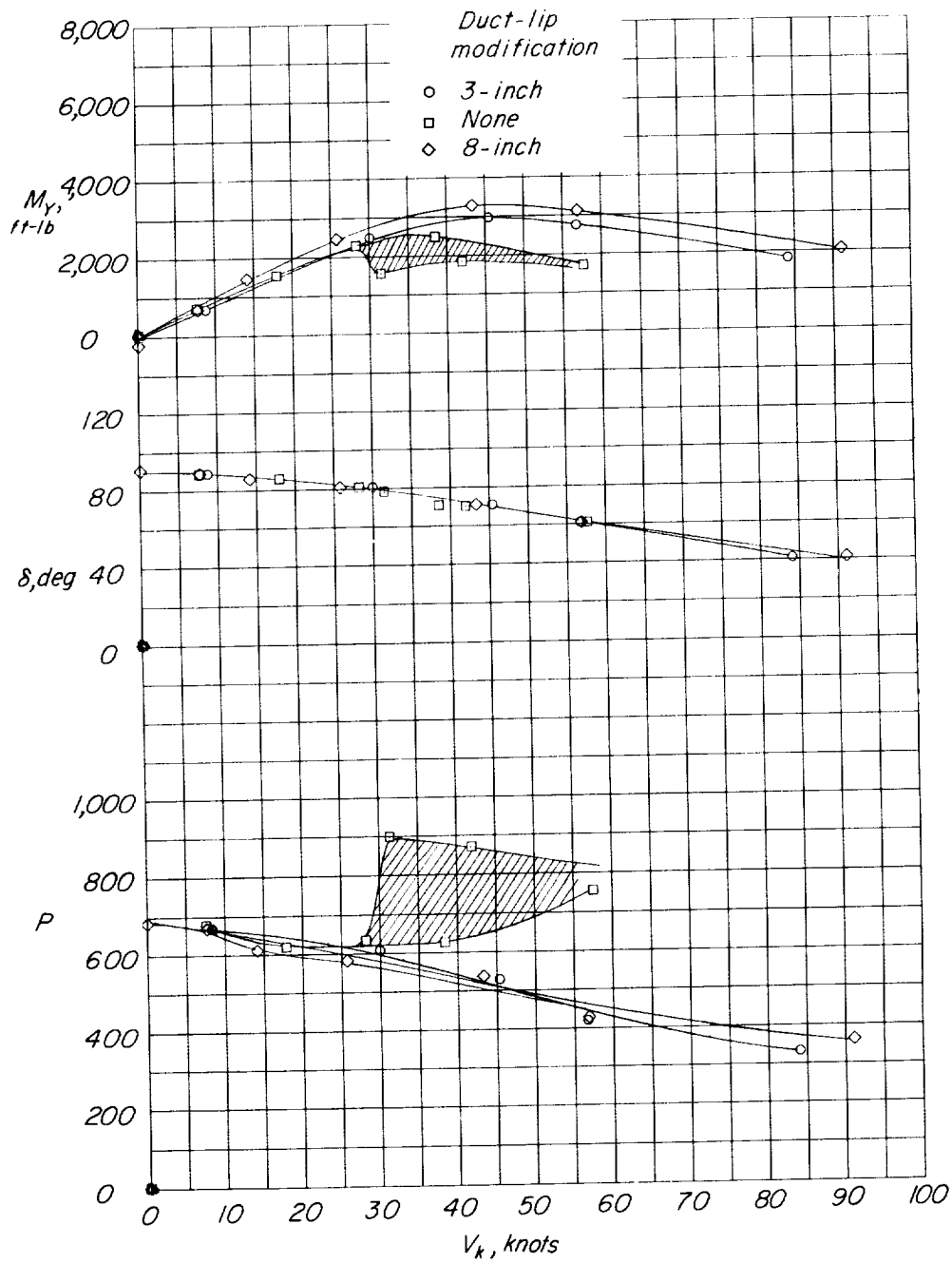

Figure 17.- Effect of duct-lip modification on the power required, duct angle, and pitching moment of a wing-tip ducted-fan configuration through a speed range. $(0g)_{\alpha=0}$ steady level flight; $\frac{h}{c} = \infty$.

L-1565

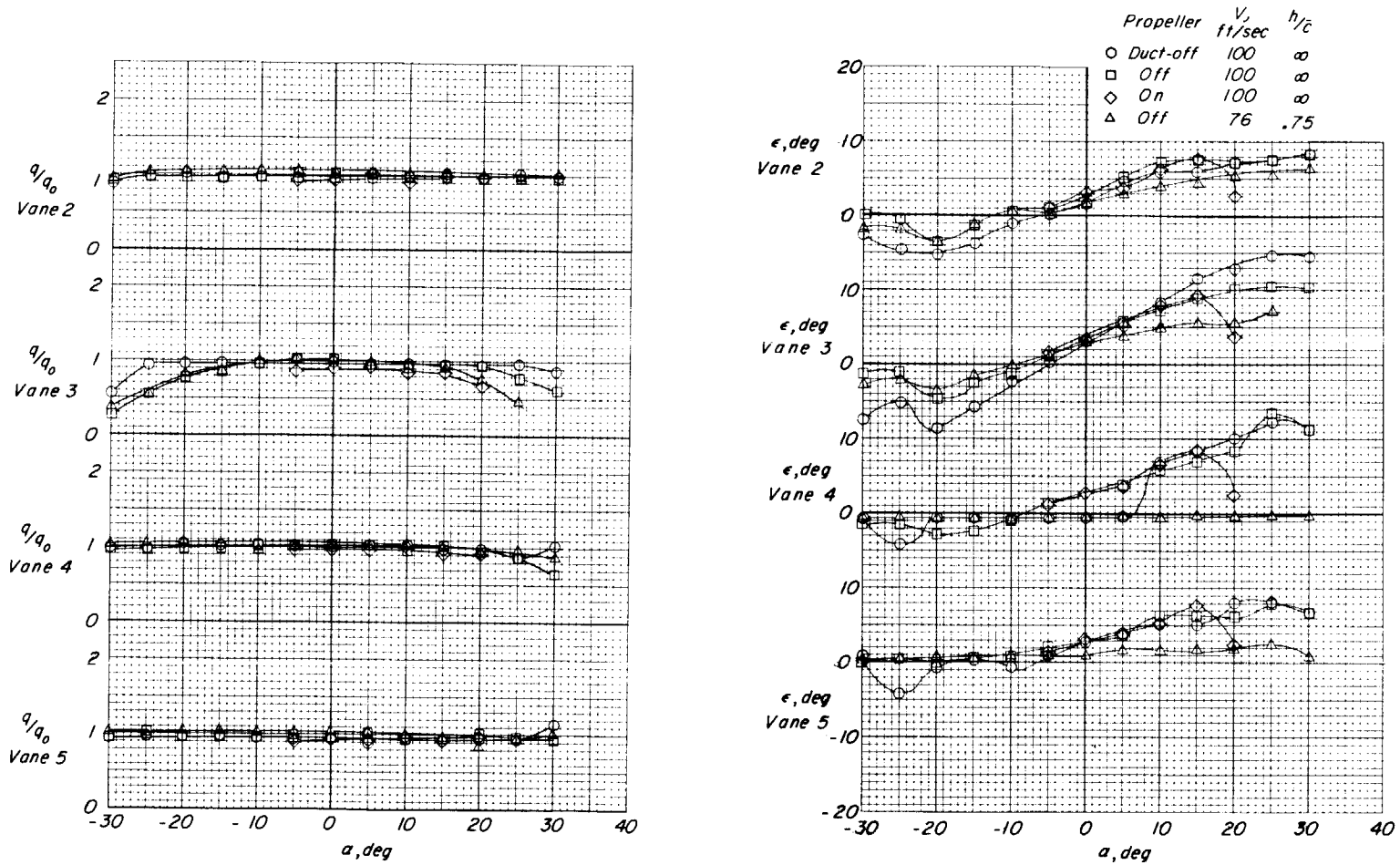

Figure 18.- Dynamic-pressure ratios and downwash angle in the region of a possible tail at high speeds in and out of the region of ground effect. Original duct; $\delta = 0^{\circ}$.

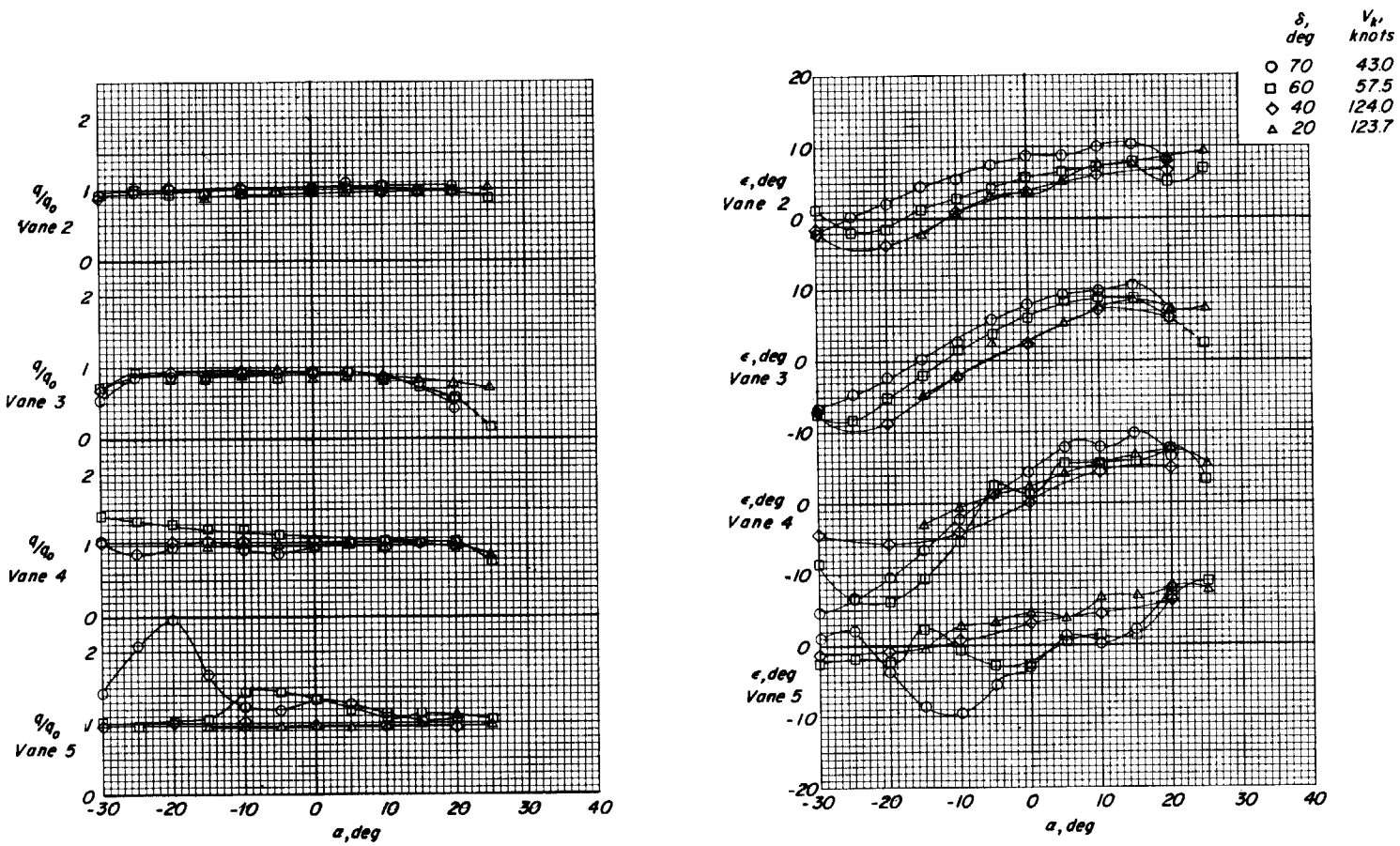

(a) $(0g)_{\alpha=0}$ steady level flight.

Figure 19.- Dynamic-pressure ratio and downwash angle in the region of a possible tail location. Original duct; $\frac{h}{\bar{c}} = \infty$.

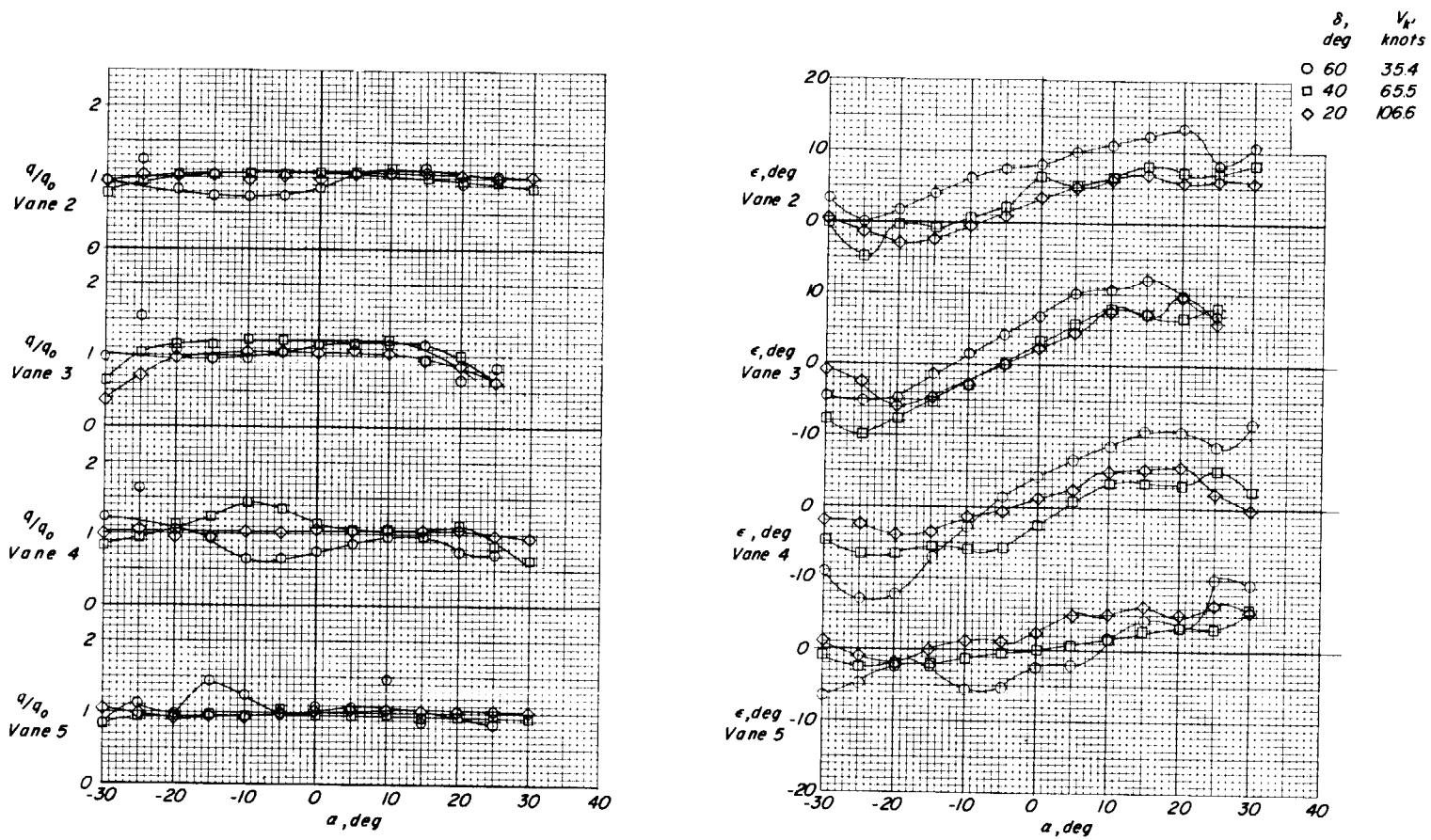

(b) $(0.313g)_{\alpha=0}$ accelerating flight condition.

Figure 19.- Continued.

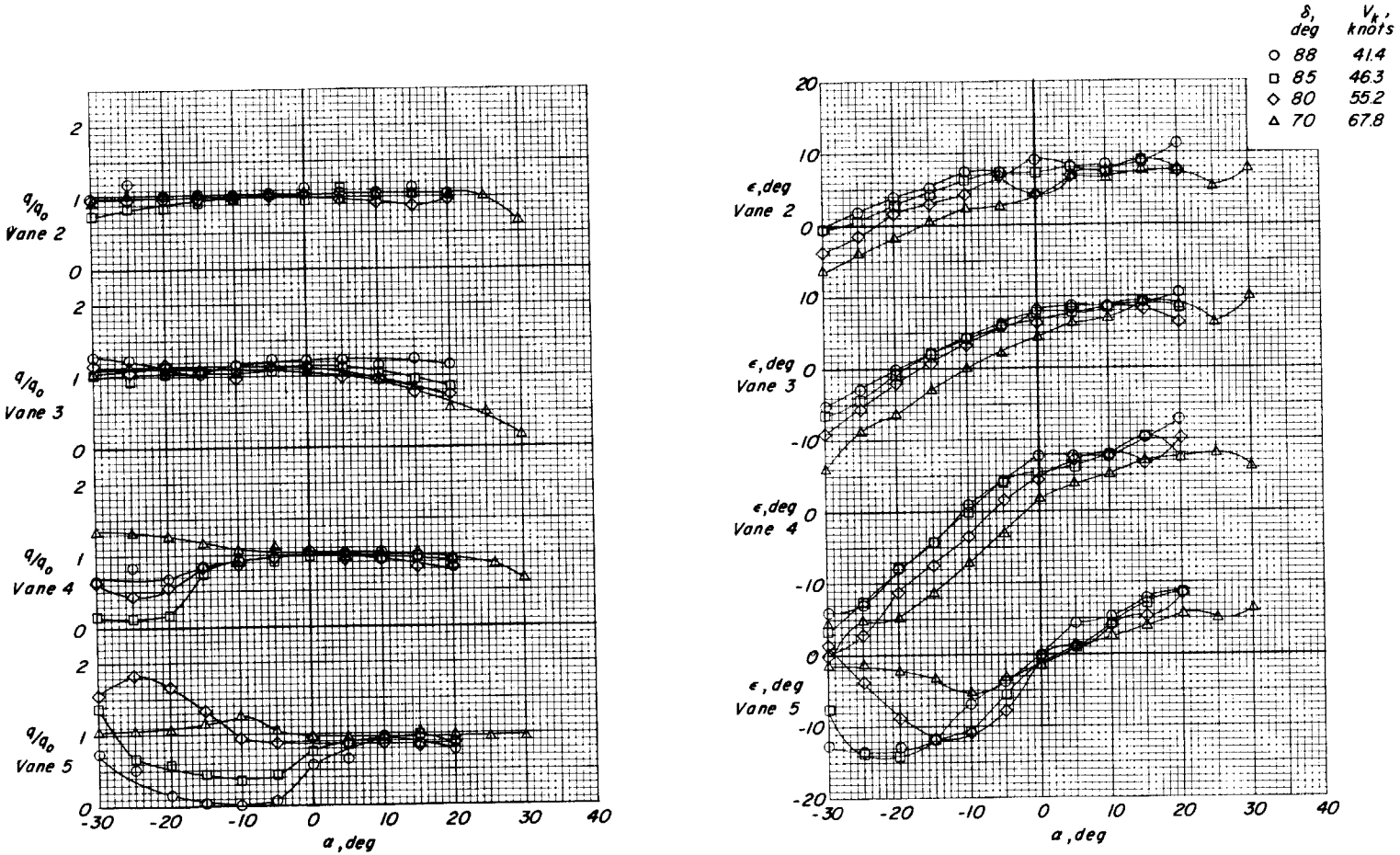

(c) $(0.313g)_{\alpha=0}$ accelerating flight condition.

Figure 19.- Concluded.

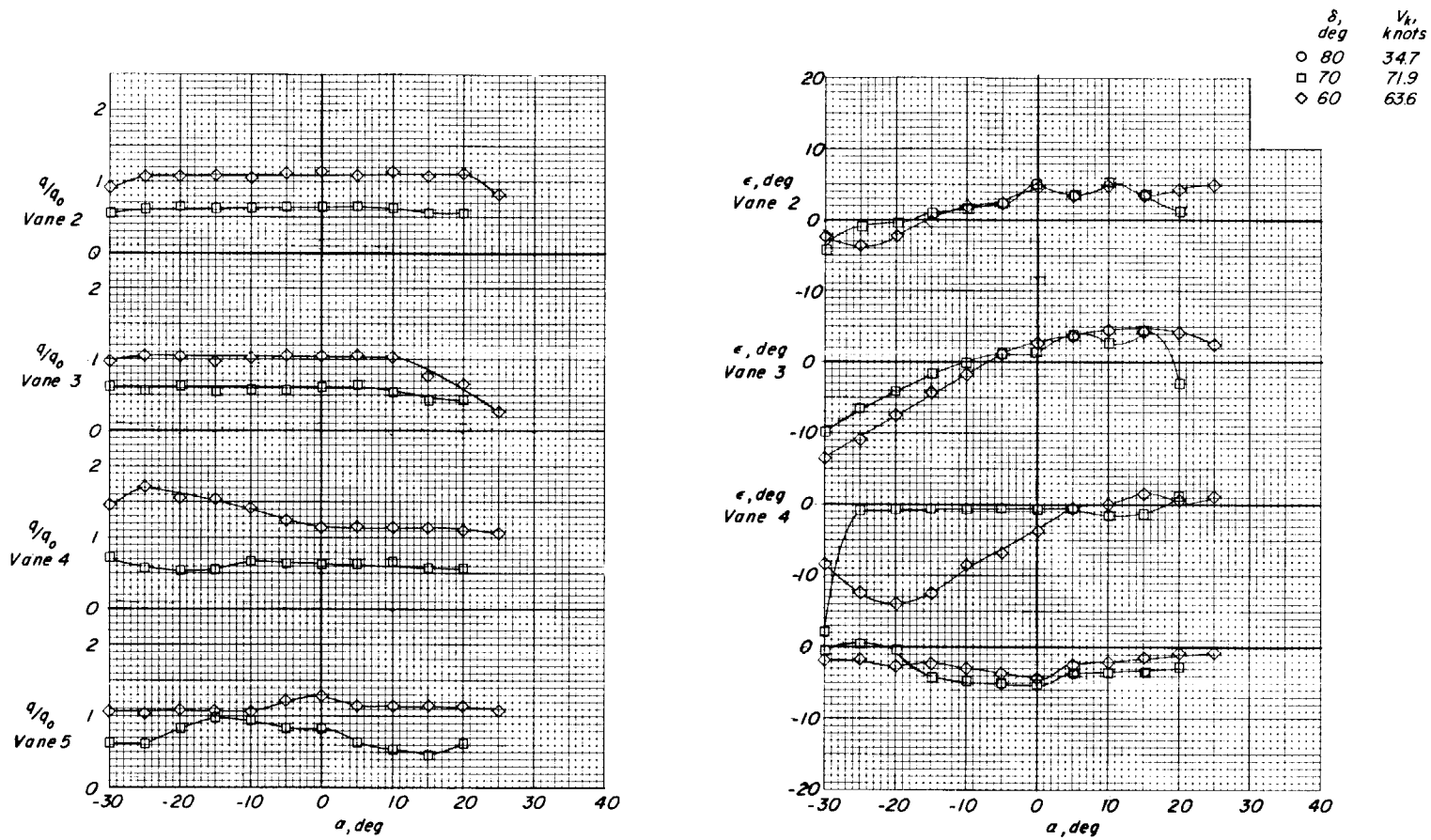

(a) $(0g)_{\alpha=0}$ steady level flight condition.

Figure 20.- Dynamic-pressure ratio and downwash angle in the region of a possible tail location. Original duct; $\frac{h}{\bar{c}} = 1.5$.

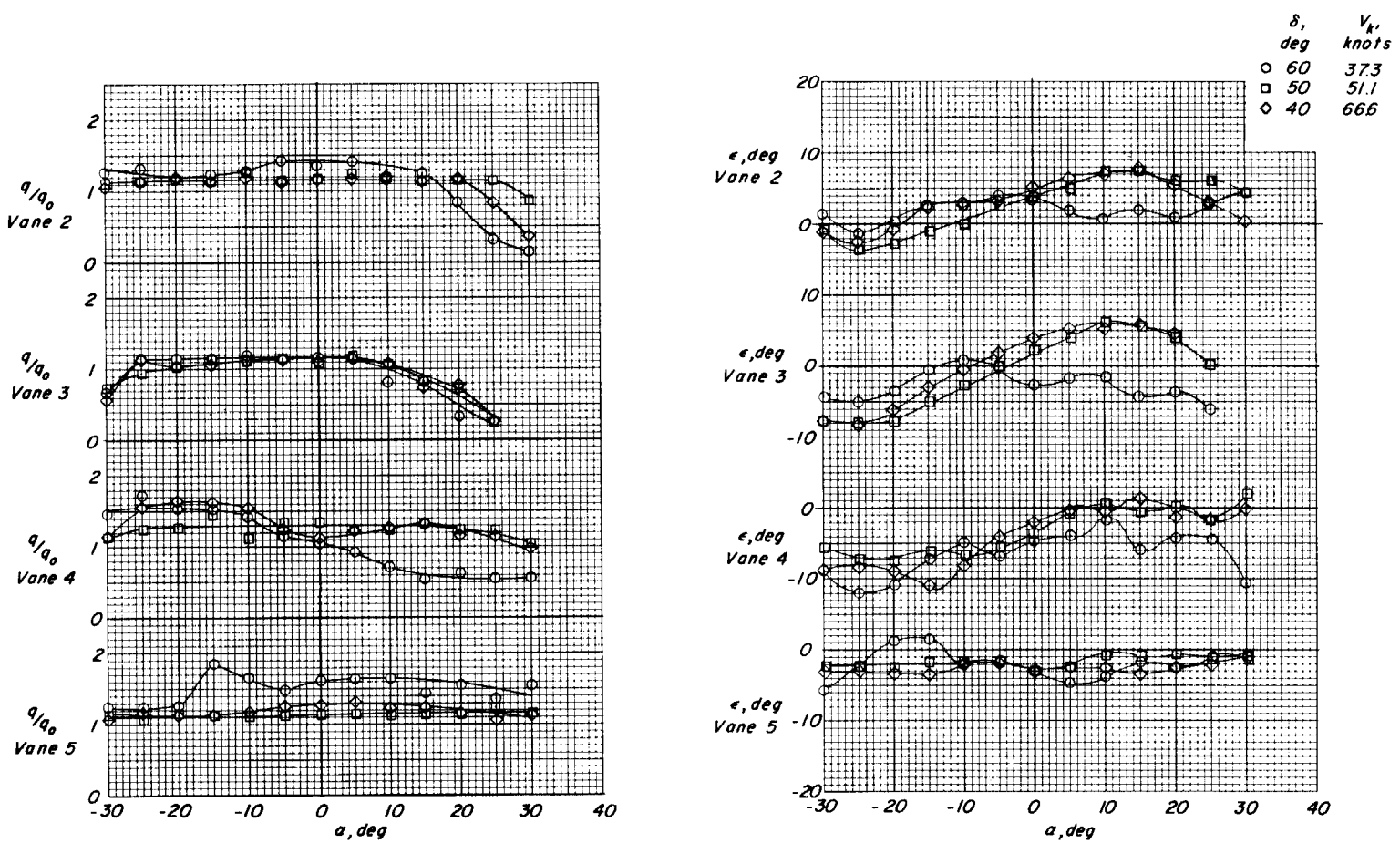

(b) $(0.313g)_{\alpha=0}$ accelerating flight condition.

Figure 20.- Continued.

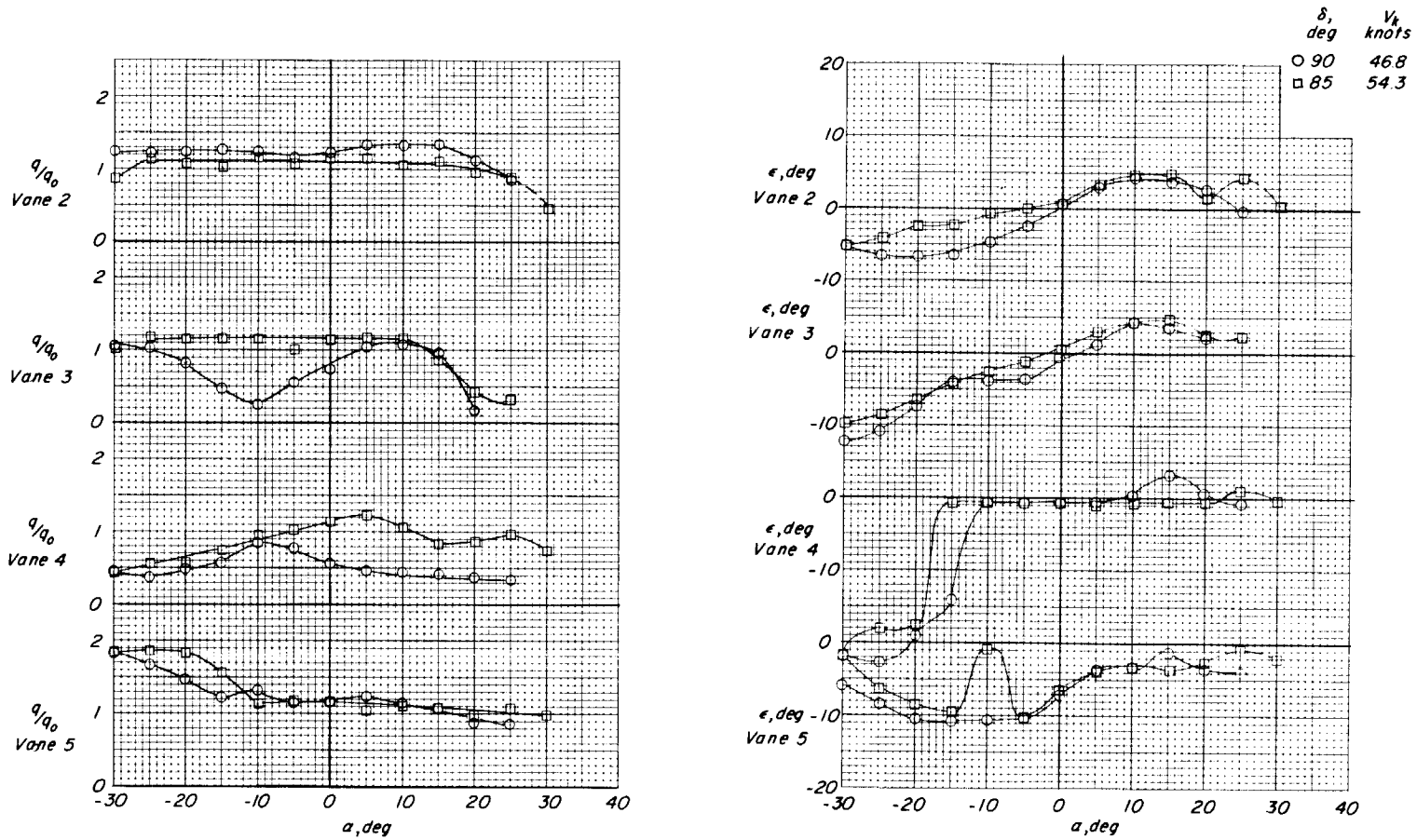

(c) $(0.313g)_{\alpha=0}$ decelerating flight condition.

Figure 20.- Concluded.

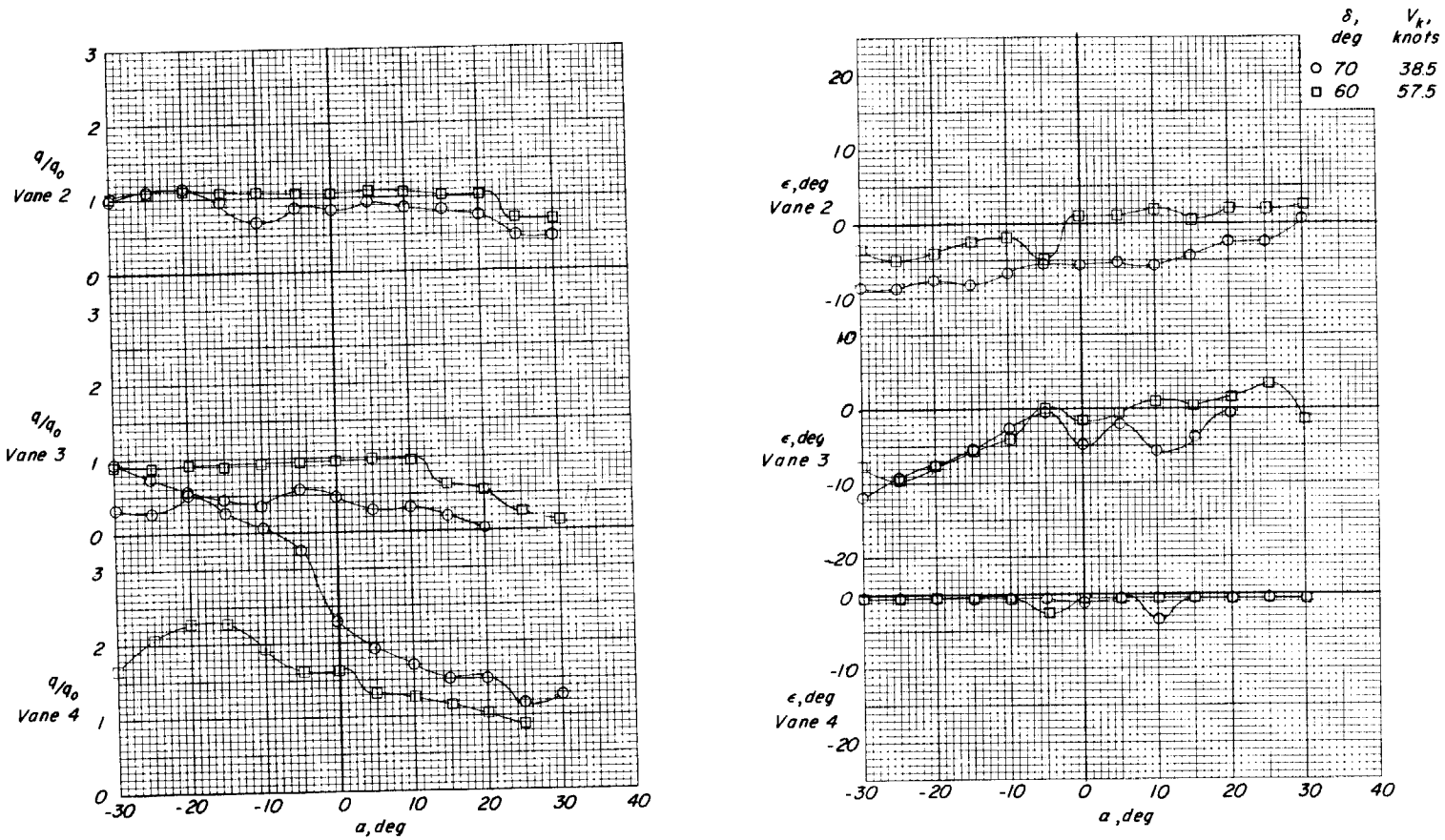

(a) $(0g)_{\alpha=0}$ steady level-flight condition.

Figure 21.- Dynamic-pressure ratio and downwash angle in the region of a possible tail location. Original duct; $\frac{h}{\bar{c}} = 0.75$.

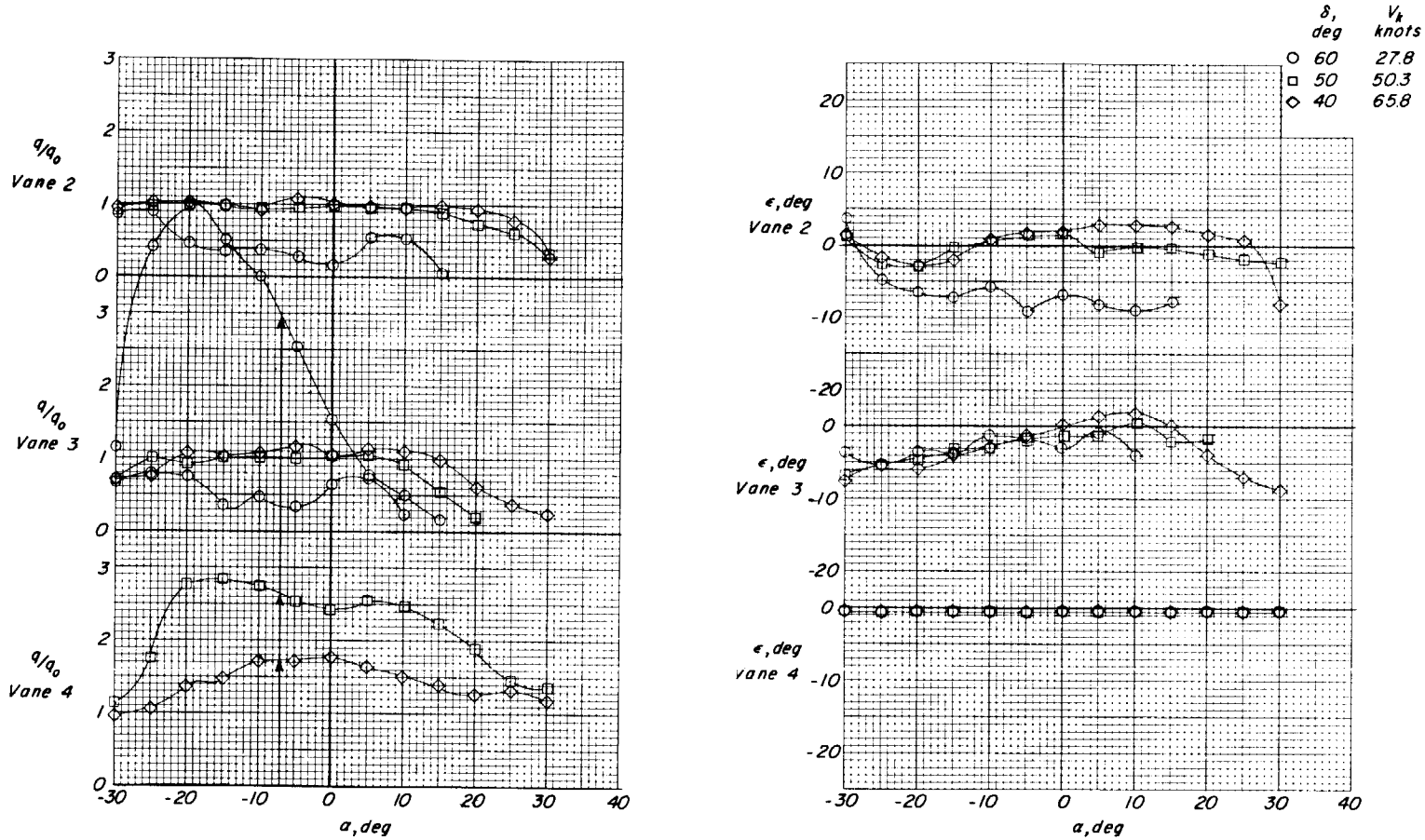

(b) $(0.313g)_{\alpha=0}$ accelerating flight condition.

Figure 21.- Continued.

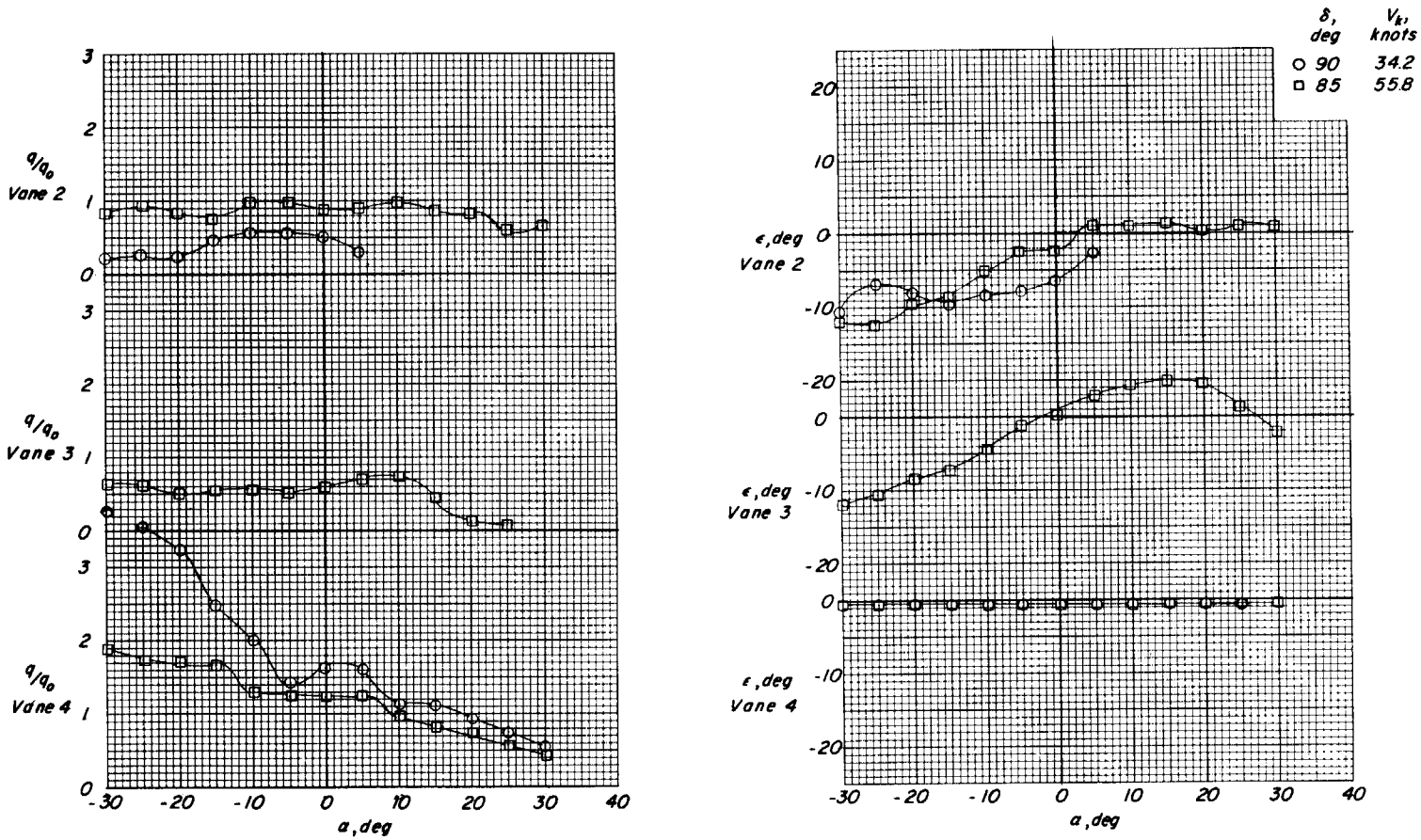

(c) $(0.313g)_{\alpha=0}$ decelerating flight condition.

Figure 21.- Concluded.

L-1565